Bubble Chamber Experiments for Strong Interaction Studies

Kasuke TAKAHASHI

KEK

National Laboratory for High Energy Physics

Oho-machi, Tsukuba-gun, Ibaraki

Bubble Chamber Experiments for Strong Interaction Studies

Kasuke Takahashi

KEK

(National Laboratory for
High Energy Physics)

1. Introductory remarks

In my lecture at this summer school, I would like to talk about what we call as "Bubble Chamber Experiment". Though there have been many interesting experiments done for so-called Weak Interaction Studies, I would like to confine myself only to the topics of strong interaction studies by using a bubble chamber.

Because of the limitation of time I have to leave the topics of bubble chamber technologies out of my talk. Accordingly we will not discuss anything, unless otherwise necessary, about for examples such questions as "what is a bubble chamber ?" or "what should we prepare for bubble chamber exposures, about incident beams, bubble chamber operating conditions, films and so on ?" Instead we simply assume that we use a very conventional hydrogen bubble chamber with a size of up to 2-meters, with a usual 20 K Gauss magnetic field. We shall start with questions "what can we see on bubble chamber films ?" and "what can we learn about Strong Interaction Physics from the events we see on the hydrogen bubble chamber films ?"

It would be however very helpful for you to know how scanning and measurement of bubble chamber films go, and to understand how measured data are processed into physically interesting results.

Scanning; Scanning is to find an event with a specific topologie or some specific topologies in which we are interested. Since scanning is the first step for film analysis, it is of essential importance in bubble chamber experiments. Scanning instructions are prepared by physicists themselves according to their experimental plans and ideas.

Scanning speed depends on scanners' skill, film qualities, topologies of the event-types interested, and scan-tables. Average scanning speed may range 50-100 frames/hour in usual πp films. Sometimes scanning and predigitization are done at the same time, in particular, for automatic measuring devices.

Measurement : Measurement is usually done by so-called measuring projectors, of which two types of digitizers are used, one is of film-plane digitizer and the other, of image-plane digitizer.. Since we need, at present bubble chamber experiment, fairly high statistical accuracy in experimental data, fast measuring apparatus is in due. Various automatic and semiautomatic measuring apparatus are thus being used and also under development for even better performance in its capabilities of speed and accuracy.

Accuracy of measurement is another important factor, since measurement of curvature of tracks means measurement of sagitta (S) over an arc of length L of the track, which directly relates to particle momentum (P) of a track. Particle momentum of a track is given by

$$P\ (\mathrm{MeV}) = 0.3\ BR/\sin\theta$$

where θ is an angle between magnetic rield $\vec{B}$ and track momentum $\vec{P}$, R, radius of curvature in cm of the projected track, and B, the magnetic field in Kilogauss. If we use projected track length l, momentum P is given as

$$P = 0.3\ Bl^2/8S\cdot\sin\theta$$

Errors in measuring momentum depend on ε_1 and ε_2 , where ε_1 and ε_2 are

ε_1 : Measurement on the table, namely measuring machine and operators (in case of manual machine).

ε_2 : Inherent errors due to films, namely multiple scattering in the chamber which is very important and systematic errors due to chamber distortion, turbulance, inaccurate setting-up of optical system, film-tilting and finite resolving power of film.

Inherent error in the photographic recording, ε_λ may be $\varepsilon_\lambda \lesssim 5\ \mu m$ on the film, and accordingly we need measuring precision with less than 5 μm.
In general automatic measuring devices are better in its measuring accuracy than in the case of manually operated measuring projectors. This is another important feature of the most automatic devices besides its speed over the manual machines.

Data Processing : Measured data are now to proceed to reconstruction of events and kinematical fitting. Three view measurements of fiducial marks and of tracks of the events are geometrically reconstructed by using geometrical programs such as THRESH[1] or TVGP (Three View Geometrical Program). This reconstruction program gives us three fundamental kinematical quantities, $1/\rho$ inverse of the radius of curvature of a track, λ , a dip angle of the track, and ϕ , its azimuthal angle. Kinematical fitting is made by using such programs as GRIND or SQUAW, for these three quantities of tracks involved in each specific event. If we define vector of measured varialbes from $1/\rho$ (W,P) λ , and ϕ , as

$$m_\mu = (P_{\mu x}, P_{\mu y}, P_{\mu z}, E_\mu),$$

energy-momentum conservation gives constraint equations,

$$\sum_\mu P_x = \sum_\mu P_y = \sum_\mu P_z = \sum (\pm) E_\mu = 0 \equiv f(m+c) \; ; \quad \text{zero vector}$$

$$\chi^2 = \tilde{C} G C + 2\alpha f = \text{minimum}$$

Where C_μ is a vector of corrections to M_μ , M_μ , a vector of measured variables, G_{ij}^{-1}, error matrix for M, and α is Lagrangian multiplier respectively. From X^2-analysis calculation gives a value of X^2-fitting for 4-constraint fit and a value for 1-constraint fit or else in various hypotheses.

Now question arises, saying "what kind of information do we get then about the measured event ?" Ideally from these kinds of measurements of bubble chamber film, we can get all kind of kinematical information on the event; namely all angles, all momenta and masses.
(Actually we very often miss a very short proton track with momentum less than about 100 MeV/c or with a large dip angle). This almost 4π-solid angle detection efficiency gives us most important advantage in bubble chamber experiment. These rather complete event-by-event kinematical information enable us to do various kinds of dynamical analysis for the events measured, such as follows;

1) Multiplicities and single particle energy spectra
2) Invariant mass distribution, Scattered mass-plot
   and Dalitz Plot ⟶ correlation among final particles. (Fig. 1)
3) Chew-Low plot ⟶ Production Angular Distribution (Fig. 2)

4) Decay angular distributions of resonance-system
   ⟶ density matrix elements,
5) Various Moments,
and
6) Polarizations of the outgoing particles.

Due to these dynamical analysis-technique and its information, Bubble Chamber Experiment has four very important features from physics point of view.
These could be summarized as follows;

1) Spectroscopies of meson and baryon resonances. By the term of spectroscopy, I mean studies of mass, spin-parity, charge-parity, isospin, branching ratio and so on.
2) Studies of $\pi\pi, K\pi$, KK scattering.
3) Studies of reaction mechanisms, namely Regge-pole exchange, diffractive process and etc. through exclusive reactions.
and
4) Inclusive Experiments.

For No. 1 feature I would like to refer you to my lecture-note in the Summer-school at Sugadaira in 1966,[2] for the Proton Synchrotron Study-Group of the University of Tokyo. At this Summer School, my talk would only be confined to what I itemized in No. 2 and No. 3 above. For inclusive-type experiment, Dr. K. Tamai will give some typical example, in connection with their recent $\pi^- p$ inclusive experiment at 8 GeV/c.

§ 2. Studies of $\pi\pi, K\pi$ and KK scatterings

2-1 Peripheral process and the one-pion-exchange mechanism (OPE)

It is well known that our present understanding of strong interactions comes largely from information on the $\pi\pi$ and $K\pi$ systems. For example, it is well understood that the $\pi\pi$ system, such as ρ^0 and f^0 mesons, and the $K\pi$ system such as K^* and K^{**} have always been a central problem in the studies of strong interaction physics.

Information on the $\pi\pi$ and $K\pi$ scattering has been mainly obtained through studies of the reactions,

$$\pi N \longrightarrow \pi\pi N \quad \cdots\cdots (1)$$

$$K N \longrightarrow K\pi N \quad \cdots\cdots (2)$$

after the famous pioneering work of Chew and Low.[3]

It is widely shown experimentally that the differential cross section of the reactions (1) and (2) have very characteristic forward peak.
The processes are known as a peripheral production. This means that the production of single pion in the process is limited mainly to the forward cone of the system.

Studies on $\pi\pi$ and $K\pi$ scattering from the analysis of the peripheral process are based on our understanding that these processes are mostly dominated by the so-called one-pion-exchange (OPE) mechanism as illustrated in Fig. 3.

Because of small pion mass, one-pion-exchange mechanism plays its most predominant role in the small $|t|$ region in these reactions, where $|t|$ is four momentum transfer squared from $N \rightarrow N'$ in the diagram. The Chew-Low extrapolation is the analysis of $\pi\pi$ or $K\pi$ scattering cross section behavior at the pion-pole in the unphysical region in the reaction shown in the diagram. Analysis with reasonable accuracy is possible due mainly to the fact that the extrapolation length from the physical region to the pion-pole in the unphysical region is relatively short because of small pion mass.

Extensive check of one-pion-exchange process has been made by G. Wolf[4] for the reactions

$$\bar{p}p \longrightarrow \bar{\Delta}^{--}\ \Delta^{++} \quad \cdots\cdots (3)$$

$$pp \longrightarrow \Delta^{++}\ n \quad \cdots\cdots (4)$$

$$\pi^+ p \longrightarrow \Delta^{++}\ \rho^0 \quad \cdots\cdots (5)$$

$$\pi^- p \longrightarrow n\rho^0 \quad \cdots\cdots (6)$$

in the very wide range of incident beam momenta from 2 to 20 GeV/c.
In particular, they analysed the reactions

$$\pi^+ p \longrightarrow p\pi^+\pi^+\pi^- \quad \cdots\cdots (7)$$

$$\pi^- p \longrightarrow p\pi^-\pi^+\pi^- \quad \cdots\cdots (8)$$

on the basis of the OPE diagram and obtained the remarkable success in

reproducing the differential cross section behaviors.

Fig. 4 shows their results.

Their conclusions can be summarized as follows; (1) the OPE contributions are quite substantial. Contributions amount to $\sim$40% of the total reaction near threshold, and go to $\sim$ 90% at 20 GeV/c. (2) the shapes of mass distributions and of distributions of other kinematical quantities are well reproduced in particular for the cases in which the contribution of one of the OPE diagrams is isolated (for example the Δ^{++} and/or ρ' events)

Direct check of the extrapolation technique, based on the OPE model was made by Colton et al,[5] in the case of the reactions of the type (4) and of the types,

$$p\,p \longrightarrow \Delta^{++}\,p\,\pi^- \quad \cdots\cdots\cdots \quad (9)$$

and

$$p\,p \longrightarrow \Delta^{++}\,n\,\pi^+\,\pi^- \quad \cdots\cdots\cdots \quad (10)$$

The experimental cross sections for these reactions at small momentum transfer were used to determine the on-mass-shell cross sections for the corresponding reactions

$$\pi^+ p \longrightarrow \Delta^{++} \longrightarrow \pi^+ p \quad \cdots\cdots\cdots \quad (4)'$$

$$\pi^- p \longrightarrow \pi^- p \quad \cdots\cdots\cdots \quad (9)'$$

and

$$\pi^- p \longrightarrow \pi^-\pi^+ n \quad \cdots\cdots\cdots \quad (10)'$$

by using the Chew-Low extrapolation. Calculated on-mass-shell cross sections are compared in terms of $\sqrt{s}$ (s is the total energy squared for the πN or $\pi\pi N$ system under considerate) with the measured on-mass-shell (physical) cross sections. They are shown in Fig. 5. Agreements are remarkable.

2-2 The Chew-Low Extrapolation.

In the analysis by Colton et al,[5] it was also found that the result of the analyses depends critically on the extrapolation fountions used.

Before going into details of individual experimental discussion, let me first describe the most basic method of the Chew-Low extrapolation. For the most basic reactions (1) and (2), the cross section in the physical region is extrapolated up to pion-pole in the unphysical region and is obtained the $\pi\pi$ or $K\pi$ scattering cross section as expressed below;

$$-F(m,-t) = \frac{2\pi}{f^2} \frac{k^2}{m\left(\frac{m^2}{4\pi}-\mu^2\right)^{1/2}} (t-\mu^2)^2 \frac{\partial^2 \sigma}{\partial t\, \partial x} \quad \cdots\cdots (11)$$

where m: mass of the $\pi^+\pi^-$ system (or $K\pi$ system), $X=m^2$

t: four momentum transfer squared ($N \to N'$)

μ: π-meson mass

f^2: pion-nucleon coupling constant

This equation can be expanded into

$$F(m,t) = \frac{t}{\mu^2}\left\{ \sigma_{\pi\pi}(m) + \sum_{n=1}^{\infty} c_n(m)(t-\mu^2)^n \right\} + \sum_{l=1}^{\infty} D_l(m)(t+\mu^2)^l \quad \cdots\cdots (12)$$

This means the $\pi\pi$ or $K\pi$ scattering cross section can be obtained by extrapolation up to the pion-pole at $t=\mu^2$ with expansion of function F (m,t) into the power series of t. The second and the third terms in the equation (12) are due to the contributions other than the pure OPE mechanism and their intereference term with the OPE amplitude.

By using these extrapolation method, most of the information on $\pi\pi$ phase shifts so far comes from reactions of the type (1).[6]

It has been shown however[7] that the $\pi N \to \pi\pi N$ type reactions suffer rather strong absorption effects. (See Fig. 6 a,b).
This absorption effect makes extrapolation difficult, though various improvements have been tried.[8] On the contrary, for the reactions of type (5) ($\pi p \to \Delta\pi\pi$), no strong absorption effect has been observed as shown by G. Wolf[4] (See Fig. 4). Accordingly better extrapolation is expected to be possilbe.

2-3 A recent example : Berkeley Experiment on $\pi^+ p \to \pi^+\pi^+\pi^- p$ at 7 GeV/c.

Recently a very interesting work on $\pi\pi$ and KK scattering has been done

by the Berkeley group[9]. As was discussed above, it is noticed that the reactions of the form $\pi N \to \pi\pi\Delta$ show pure OPE mechanism without any absorption correction, and are considered to be very suitable for $\pi\pi$ scattering extrapolation analysis. With a special attention to this point, Berkeley people have measured the 700 thousand exposures (approximately 45 $\mu b/\mu b$ equivalent pictures) taken at the SLAC-LBL 82-inch hydrogen bubble chamber with a π^+ beam at 7.1 GeV/c.

For reaction $\pi^+ p \to \Delta^{++}\pi^+\pi^-$, 245 thousand 4-prong events are measured for which at least one heavily ionizing track is observed. 68 thousand events of $\pi^+ p \to \pi^+ p \pi^+\pi^-$ are observed. Selections are also made for the events of the form $\pi^+ p \to \pi^+ p K^+ K^-$, with a 10% ambiguities for the K^+K^- events due to $\pi^+\pi^-$ contamination. They have selected events of the reactions

$$\pi^+ p \longrightarrow \Delta^{++}\pi^+\pi^- \qquad 32{,}000 \text{ events}$$

$$\longrightarrow \Delta^{++} K^+ K^- \qquad 740 \text{ events}$$

where Δ^{++} means M $\pi^+ p < 1.4$ GeV. Restriction for $t_{p\Delta}$ (four momentum transfer squared from target proton to produced Δ^{++}, see Fig. 7) was superimposed as $t'_{p\Delta} = |t - t_{min}| < 0.1$ (GeV/c)^2.

This reduces ambiguities between two π^+ in the final state and also to enhance the ratio of OPE-events to the background[4]. Since they used special criteria for identifying a proton track with observed heavy ionization at Spiral Reader output pulse height, they seem to have good selection of proton. It may sometime happen however that because of two π^+ tracks, both $\pi^+ p$ combinations drop in the above Δ^{++} mass region. In case of this sort of ambiguities, they selected the $\pi^+ p$ combination with the amallest $t'_{p\Delta}$. Though identical selection criteria were used for the $\Delta^{++}K^+K^-$ reaction, no significant contamination of the $\Delta^{++}K^+K^-$ events by the $\Delta^{++}\pi^+\pi^-$ events seemed to be found. This much less ambiguity in selecting the events may mean that the $\Delta^{++}\pi^+\pi^-$ type reaction has better property for analysis of $\pi\pi$ scattering through the OPE than the reaction of the form $\pi N \to \pi\pi N$[4].

The mass resolution of the $\pi^+\pi^-$ system near 1000 MeV in this experiment is reported to be $\pm$ 6.5 MeV (HWHM), and it is reported to be fairly independent on the decay angle of the $\pi^+\pi^-$ system. (Fig. 8)

As usual, invariant mass distribution of $\pi^+\pi^-$ system and spherical harmonic moments of the system are studied. Three sharp effects are observed near 980 MeV. They report these effects as follows:

(1) The $\langle Y_1^0 \rangle$ moment shows very strong discontinuity at 980 MeV. The effect must be due to rapid change in either the S-wave or the P-wave amplitude, since below 1100 Mev, the $\langle Y_1 \rangle$ moment is primarily due to the interference effect between S-and P-waves.

(2) There is a sharp rise in $\langle Y_2^0 \rangle$ near 980 MeV. Since the $\langle Y_2^0 \rangle$ is mostly dominated by the contribution proportional to $\frac{|P|^2}{(|S|^2+|P|^2)}$, this means either increasing P-wave amplitude or the decreasing S-wave.

(3) In the mass distribution, a shoulder between 910 MeV and 950 MeV, a sharp drop between 950 MeV and 980 MeV, and a flat region above 980 MeV are observed. The sharp drop in the mass distribution, which combined with the $\langle Y_1 \rangle$ and $\langle Y_2 \rangle$ information implies that the observed effect is in the S-wave amplitude.

In order to elaborate their analysis of the $\pi\pi$ system, they have made further analysis with the technique of the Chew-Low extrapolation, since it is well convinced that the reaction of the form $\pi^+ p \to \pi\pi\Delta^{++}$ is quite suitable for extrapolation. In this reaction, there is some disadvantage due to a little large $|t_{p\Delta}|_{min.}$ compared with the $\pi N \to \pi\pi N$ case. They used a conventional type of Chew-Low linear extrapolation with a form factor correction of the type by Dürr and Pilkuhn[10].

Since the reaction is considered to be dominated by one pion-exchange, the amplitude for the reaction $\pi^+ p \to \pi^+\pi^-\Delta^{++}$ is of the form (ignoring effects of absorption);

$$A(s,t) \propto \frac{\langle \pi^+ p | T | \pi^+ p \rangle \cdot \langle \pi^+\pi^- | T | \pi^+\pi^- \rangle}{t - \mu^2} + X \qquad \cdots\cdots (13)$$

where X stands for processes not produced by pion-exchange, namely, A_2-exchange, $\pi^+ p \to A_2 p$, $\pi^+ p \to \pi^+ N^{*+}$, etc. When $t \to \mu^2$ the first term diverges while X remains finite. Accordingly by extrapolating to $t=\mu^2$, one hopes to remove off-shell effects and non-pion-exchange contributions. The analysis then becomes simpler in the sense that a standard phase shift analysis may be attempted.

This simplicity is however offset by the uncertainties in extrapolation procedures and the large increase in the statistical errors. (We need to divide the data in cells of t and $m_{\pi\pi}$). Uncertainty becomes larger, the higher the mass because $|t|_{min.}$ incerases (see Fig. 2, 5).

Now the differential cross section for the process $\pi^+p \to (\pi^+\pi^-)(\pi^+p)$ is given by;[9),4)]

$$\frac{d^3\sigma}{dt\, dM\, dm} = \frac{1}{4\pi^3 P_I^2 E^2} (m^2 q_t \sigma_{\pi\pi}) \frac{G^2(t)}{(t-\mu^2)^2} (M^2 Q_t \sigma_{\pi p}) \qquad \cdots\cdots\cdots (14)$$

where

P_1 = c.m. momentum, E = c.m. energy,

m = $\pi^+\pi^-$ invariant mass, M = π^+p invariant mass,

G(t) = form factor (=1 at π-pole), μ = pion mass,

$\sigma_{\pi\pi}$ = $\pi^+\pi^-$ cross section, $\sigma_{\pi p}$ = π^+p cross section

q_t = virtual pion momentum in the $\pi^+\pi^-$ rest frame

Q_t = incoming proton momentum in the π^+p rest frame.

If we define q and Q for later use, as

q = outgoing π^+ momentum in $\pi^+\pi^-$ rest frame

Q = outgoing proton momentum in π^+p rest frame,

where we have,

$$q_t = \sqrt{\frac{(m^2+\mu^2-t)^2}{4m^2} - \mu^2}, \qquad Q_t = \sqrt{\frac{(M^2+m_p^2-t)^2}{4M^2} - m_p^2}$$

$$q = \sqrt{\frac{m^2}{4} - \mu^2}, \qquad Q = \frac{1}{2M}\left\{[M^2-(m_p+\mu)^2][M^2-(m_p-\mu)^2]\right\}^{1/2} \qquad \cdots\cdots (15)$$

Extrapolation is made by calculating first;

$$\sigma_{OPE} \equiv \frac{1}{4\pi^3 P_I^2 E^2} \int_{m'}^{m^2} dm \int_{t'}^{t^2} dt \int_{M'}^{M^2} dM \cdot m^2 q_t \frac{G(t)^2}{(t-\mu^2)^2} M^2 Q_t \sigma_{\pi p} \qquad \cdots\cdots (16)$$

Integration of (14) is made by setting $\sigma_{\pi\pi}$ = 1 mb as a unit and $\sigma_{\pi p}$ is the physical $\pi^+p \to \pi^+p$ scattering cross section. Then we make fitting the function F(m, t) to a polynomial in t by the formula

$$F(m,\ t) = \left(\int_{m_1}^{m_2} dm' \int_{t_1}^{t_2} dt' \int_{M_1}^{M_2} dM \ \frac{d^3\sigma}{dt'\, dM\, dm} \right) \Big/ \sigma_{OPE} \quad \cdots\cdots (17)$$

where the function F(m, t) is calculated by taking the experimental cross section averaged over a bin in (t, m, M) and divided by σ_{OPE}, t and m are $m=(m_1 + m_2)/2$ and $t=(t_1 + t_2)/2$ and the cross section for $\pi^+\pi^-$ is then given by $\sigma_{\pi\pi}(m)=F(m,\ t=\mu^2)$.

In general, for this procedure one needs higher order polynomials in t to obtain good results.[6),11)]
Berkeley people, however, made successful extrapolation by using only a linear or at most quadratic forms, but with a help of Dürr-Pilkuhn (DP) form factors for modifying σ_{OPE}. When we use the DP form factors, the disadvantage is that we must know in advance the amounts of each partial wave present.
The effect of the DP form factors however is not so big and so a rough estimation usually works adequate.

The DP form factor can be expressed by replacing q t with[10),4)]

$$\left.\begin{array}{ll} q & \text{for S-wave} \\ \left(\frac{qt}{q}\right)^2 \cdot \left(\frac{1 + R_P^2 q^2}{1 + R_P^2 q^2 t}\right) \cdot q & \text{for P-wave} \\ \left(\frac{qt}{q}\right)^4 \cdot \left(\frac{9 + 3R_d^2 q^2 + R_d^4 q^4}{9 + 3R_d^2 q^2 t + R_d^4 q^4 t^2}\right) q & \text{for d-wave} \end{array}\right\} \quad \cdots\cdots (18)$$

and for the Δ^{++} vertex, Q_t is replaced by

$$Qt \longrightarrow \frac{(M + m_p)^2 - t}{(M + m_p)^2 - \mu^2} \cdot \left(\frac{Qt}{Q}\right) \cdot \frac{1 + R_\Delta^2 Q^2}{1 + R_\Delta^2 Qt^2} \cdot Q \quad \cdots\cdots (19)$$

for G(t), it is usually expressed by a slowly varying function;
such as [4)]

$$Q(t) = \frac{C - \mu^2}{C + t} \qquad \text{where } C=2.29 \pm 0.27\ (\text{GeV})^2$$

For calculating σ_{OPE}, $R_\Delta = 4.0\ \text{GeV}^{-1}$, $R_p = 8.2\ \text{GeV}^{-1}$ and $R_d = 14.0\ \text{GeV}^{-1}$ are used and the experimental values $\sigma_{\pi p}$ are taken from the data by Carter et al.[9),12)]

Then a least squares fit is made to,

$$F(m, t) = a + bt \qquad \cdots\cdots\cdots\cdots (20)$$

to determine a and b for various mass bins. Extrapolations were tried for many different t-intervals.

To extrapolate the $\langle Y_L^* \rangle$ moments they simply did caluculation of the form;

$$\langle Y_L^* \rangle (m, t) = \left(\sum_{i=1}^{N\text{-events}} Y_{L,i}^* \right) \Big/ N \qquad \cdots\cdots\cdots (21)$$

where N=number of events in (m, t) cell, and fit $\langle Y_L^* \rangle (m, t)$ for each m to a function a+bt. The $\pi\pi \langle Y_L^* \rangle$ is assumed to be equal to $\langle Y_L^* \rangle (m, \mu)$. Since the moments are normalized, one can neglect kinematic factors. The validity of the extrapolation procedure can be checked by looking at Y_l^0 for the π^+p vertex as a function of π^+p and $\pi^+\pi^-$ mass. They should show no dependence on $\pi^+\pi^-$ mass.

The extrapolated mass distribution and the spherical harmonic moments $\langle Y_l^* \rangle$ of the $\pi^+\pi^-$ system are found to be very similar to the data for $|t_{p\Delta}'| \leq 0.1$ (GeV/c)^2, both of which are given in Fig. 9~Fig. 13 for comparison.
We observe that only noteworthy difference is at the $\langle Y_3^* \rangle$ moment. Again the most striking features are seen in the $\pi^+\pi^-$ mass system near 980 MeV and the $\langle Y_1^* \rangle$ and the $\langle Y_2^* \rangle$ moments in the region of 900-1000 MeV.

In connection with their interpretation of the observed striking features, they have analysed the K^+K^- spectrum with 740 events of $K^+K^-\Delta^{++}$. The spectrum is shown in Fig. 9 (c). Study of cross section ratio between the ($\pi^+\pi^-\Delta^{++}$) events and the ($K^+K^-\Delta^{++}$) is also made. We observe in the figure a very sharp rise in the K^+K^- mass near 980 MeV, threshold energy for K^+K^- system. This feature of the K^+K^- spectrum is most naturally interpreted that a rapid change in the S-wave is associated with the $K\bar{K}$ threshold. These $\pi^+\pi^-$ and K^+K^- cross sections are checked with its unitarity values.

After the evaluation of the $\pi^+\pi^- \to \pi^+\pi^-$ and $\pi^+\pi^- \to K^+K^-$ cross sections, we are ready to make analysis of partial wave amplitudes for $\pi^+\pi$ scattering.

The partial wave amplitudes for $\pi^+\pi^-$ scattering may be written as[9];

$$S = \frac{2}{3} T_0^{\circ} + \frac{1}{3} T_0^{2}, \quad P = T_1^{\prime}$$
$$D = \frac{2}{3} T_2^{\circ} + \frac{1}{3} T_2^{2}, \quad F = T_3^{\prime} \qquad \text{(22)}$$

where

$$T_L^{I} = \frac{1}{2i} \left(\eta_L^{I} e^{2i\delta_L^{I}} - 1 \right) \qquad \text{(23)}$$

Upper indices denote I-spin and lower indices angular momentum. The cross section and the $\langle Y_L^{\circ} \rangle$ moments are, in terms of the above amplitude;

$$\sigma_{\pi\pi} = 4\pi\lambda^2 \left(|S|^2 + 3|P|^2 + 5|D|^2 + 7|F|^2 \right) \qquad \text{(24)}$$

and

$$\langle Y_1^{\circ} \rangle = \left(\sqrt{\tfrac{3}{\pi}} \operatorname{Re}(S^{*}P) + 2\sqrt{\tfrac{3}{\pi}} \operatorname{Re}(P^{*}D) + 3\sqrt{\tfrac{3}{\pi}} \operatorname{Re}(D^{*}F) \right) \frac{4\pi\lambda^2}{\sigma_{\pi\pi}},$$

$$\langle Y_2^{\circ} \rangle = \left(\frac{3}{\sqrt{5\pi}} |P|^2 + \sqrt{\tfrac{5}{\pi}} \operatorname{Re}(S^{*}D) + \frac{5}{7}\sqrt{\tfrac{5}{\pi}} |D|^2 + \frac{9}{\sqrt{5\pi}} \operatorname{Re}(P^{*}F) + \frac{14}{3\sqrt{5\pi}} |F|^2 \right) \frac{4\pi\lambda^2}{\sigma_{\pi\pi}},$$

$$\langle Y_3^{\circ} \rangle = \left(\frac{9}{\sqrt{7\pi}} \operatorname{Re}(P^{*}D) + \frac{4}{3}\sqrt{\tfrac{7}{\pi}} \operatorname{Re}(D^{*}F) + \sqrt{\tfrac{7}{\pi}} \operatorname{Re}(S^{*}F) \right) \frac{4\pi\lambda^2}{\sigma_{\pi\pi}},$$

$$\langle Y_4^{\circ} \rangle = \left(\frac{15}{7} \cdot \frac{1}{\sqrt{\pi}} |D|^2 + \frac{4}{\sqrt{\pi}} \operatorname{Re}(P^{*}F) + \frac{21}{11\sqrt{\pi}} |F|^2 \right) \frac{4\pi\lambda^2}{\sigma_{\pi\pi}},$$

$$\langle Y_5^{\circ} \rangle = \frac{50}{3\sqrt{11\pi}} \operatorname{Re}(D^{*}F) \frac{4\pi\lambda^2}{\sigma_{\pi\pi}},$$

$$\langle Y_6^{\circ} \rangle = \frac{350}{33\sqrt{13\pi}} |F|^2 \frac{4\pi\lambda^2}{\sigma_{\pi\pi}} \qquad \text{(25)}$$

What we want to determine are inelasticity η_L^I and phase shift δ_L^I for each wave with I=0 and I=2 or I=1 correspondingly. Then the total number of parameters to be determined at each value of $m_{\pi\pi}$ is 12, assuming partical waves up to L=3 are important. Accordingly it is not possible to determine

them by an energy independent analysis using the $\pi^+p \to \pi^+\pi^-\Delta^{++}$ alone, since we have only seven constraints (six moments and the cross section). In order to extract phase shifts and inelasticities we parametrize them as functions of $\pi\pi$ mass and then do a least-square fit to the moments and the cross section. For the Berkeley group it was also necessary to make some model parametrization for $\pi\pi$ scattering.

Protopopescu et al[9] made various parametrizations and analysed the scattering. Here we leave the details of their parametrization for further reference and give only their conclusion.

For example, taking the following parametrization like

d-wave ; the f°-meson with M_f=1270 MeV, Γ_{f°=180 MeV

p-wave ; the ρ-meson with M =770 MeV, Γ_{ρ°=140 MeV

s-wave ; (a) the S^*-meson with coupling to both $K\bar{K}$ and $\pi\pi$, but no coupling to other channels.

(b) an elastic s-wave background represented by a constant phase shift δ.

With these parametrization, they draw their conclusion on the anomalous behavior of s-wave amplitude near 1 GeV.*) The s-wave phase shift at 900 MeV is close to 90° and it moves very rapidly to 180° at 990 MeV. (Table I) They conclude their data near $K\bar{K}$ threshold can then be parametrized by an S^* resonance ($J^{PC} = 0^{++}$, $L^G = 0^+$) at 990 MeV which couples to both $\pi\pi$ and $K\bar{K}$, but more strongly to $K\bar{K}$. Very similar treatment for $\pi\pi$-phase shift analysis with $K\bar{K}$ threshold effect has been done by Y. Fujii and M. Kato.[13]

§ 3 Studies of Reaction Mechanism

3-1 Nature of Diffractive Process

One of the most fundamental problem in strong interaction is a problem of the so-called diffractive process in which a Pomeranchuk pole may play

---

*) For $\pi^\circ\pi^\circ$ scattering similar behavior around 900 MeV seems to be observed. This may give additional constraints in the analysis of $\pi\pi$-phase shifts. (Review talk by R. Diebold at the Batavia Conference, September, 1972) We thank Dr. Y. Hara for his private communication.

a cetnral role. Pomeranchuk exchange is conjectured in order to explain the observed constancy of total cross sections of fundamental hadronic reactions at high energy, NN, $\bar{N}N$, $\pi^{\pm}N$, $K^{\pm}N$ and so on.
A Pomeranchuk pole is considered to have properties which vacuum may have, namely isoscalar and $J^P = 0^+$, and to conserve all internal quantum numbers in the exchanged process.

It should be said, however, that our understanding on the problem of diffraction process or about Pomeranchuk exchange has been quite meager. It is only very recently that various experimental attacks to probe this question, have been made. Some recent bubble chamber experiments are among others quite interesting from this point of view.

Examples are as follows;

(i) Experiments on the process $\gamma p \to \rho^0 p$ [14),15),16)]

(ii) Experiments on the processes, such as $\pi p \to A_1 p$, $A_3 p$ and $Kp \to Qp$ etc.[17)]

(iii) Various inclusive experiments[18)]

3-2 Photoproduction of vector mesons with polarized photons

——— SLAC—Berkeley Experiment, for example ———

Today, we shall talk about only one example, which falls into category (i). The experiment is carried out under continueing series of experimental projects done by the SLAC-Berkeley Bubble Chamber Group.

The process of

$$\left.\begin{array}{l} \gamma p \to \rho^0 p \\ \qquad\quad \hookrightarrow \pi^+\pi^- \end{array}\right\} \cdots\cdots\cdots (25)$$

is considered to be one of the typical process in which Pomeranchuk exchange plays a dominant role. To know how the process goes, its S-dependence, and properties of its helicity amplitudes, is their (SLAC-Berkeley Groups) experimental purpose.

They have so far made series of exposures of total more than 2 million pictures by using the SLAC-LBL 82" Bubble chamber at various incident photon energies from 2 GeV upto 9 GeV, with monochromated polarized photon beams. Their pictures are equivalent to 90, 150 and 250 events/μb at 2.8, 4.7 and

9.3 GeV respectively.

Experimental details are rather straight forward, if you could allow me to skip over the detailed story about how to make a polarized monochromatic gamma rays from accelerated electron beams at the SLAC 2-mile accelerator.[16] Measurements are done both at the SLAC and Berkeley with their Spiral Reader measuring system. Cross sections are obtained by comparing the number of event, to the number of $e^+ e^-$ pairs found in the same fiducial volume and using the pair production cross sections known to 0.5% for flux normalization.

After standard analysis of the measured events of 3-prong topology, they have made very detailed and careful studies of the invariant mass distribution of $\pi^+\pi^-$ system, its production angular distributions of pions and its spin density matrix elements in various reference frames.

Let us first see the dipion ($\pi^+ \pi^-$) spectrum for all events observed in the reaction

$$\gamma + p \longrightarrow \pi^+ + \pi^- + p \qquad \cdots\cdots\cdots (26)$$

at 9.3 GeV (Fig. 14). We see that any background is almost negligible under the clear ρ° signal and the reaction (26) occurs predominantly through the reaction (25). In the dipion mass, we note two striking features, the low mass skewing of the ρ° resonance shape and almost complete absence of a high mass tail which we should expect to see. To explore these problems, they have made various analyses.

The first measurement they made is that of contributions of natural parity exchange σ_N and unnatural parity exchange σ_U to the ρ° production cross section σ. For forward ρ°, the polarization dependence in the matrix element for exchange of any trajectory in the natural parity sequence ($P = (-1)^J$, P is parity and J, its spin) will involve the polarization vector, $\vec{\varepsilon}$ of γ and ρ° in the from $\vec{\varepsilon}_\gamma \cdot \vec{\varepsilon}_\rho$. For unnatural parity exchange ($P= (-1)^{J+1}$), the form must be pseudoscalar and of the form $(\vec{\varepsilon}_\gamma \times \vec{k}) \cdot \vec{\varepsilon}_\rho$(here $\vec{k}$ is momentum vector of photons). These lead to the angular distributions in the ρ° rest frame

$$\frac{d\sigma_N}{d\Omega} \propto \sin^2\theta \cos^2\psi \qquad \cdots\cdots\cdots (27)$$

$$\frac{d\sigma_U}{d\Omega} \propto \sin^2\theta \sin^2\psi \qquad \cdots\cdots\cdots (28)$$

where θ is the angle of the π^+ in the ρ° rest frame with respect to the c.m.s. ρ° direction and ψ is the azimuth of the π^+ with respect to the photon polarization plane. (see Fig. 15) Thus the natural and unnatural cross section are separable, by defining the parity asymmetry

$$P_\sigma = \frac{\sigma_N - \sigma_U}{\sigma_N + \sigma_U}$$

Fig. 16 shows one of examples for 1457 events of reaction (26) at $E_\gamma = 4.7$ GeV. It is evident that natural parity exchange dominates the process. The isotropic parts we observe have been consistently explained as due to contributions coming from background and the unpolarized beam component.

It may be worth noticing that in the bubble chamber data, we can isolate contributions to parity asymmetry, P_σ due to helicity flip because it has a $\cos^2\theta$ dependence (see scatter-plot of $\cos\theta$-ψ distribution in Fig. 15). These are lost in general in the data of counter experiments, where measurements are usually done of the cross section for symmetric (namely $\theta = \pi/2$) ρ° decay at two azimuthal angle $\psi = 0$ or $\psi = \pi/2$, obtaining so-called $\sigma_{/\!/}$ and $\sigma_\perp$ respectively. This point is a quite advantage of bubble chamber data as I stressed in §1.

Another very important feature we can study in this experiment is to get information on the helicity state involved in this reaction which is very importatn to know how Pomeranchuk pole behaves in helicity amplitude of the diffractive process. We can see the effect of ρ helicity flip as a sign of longitudinally polarized ρ. Namely we analyse the angular distribution of ρ° decay and its density matrix elements. Since we know the pion pair system are in a predominantly P-state, to which we refer as ρ°, we could follow the formalism of Thews[19] and Schilling et al[20] for vector meson production by polarized photons.

Let me explain this point a little in detail, refering to Ref. 16). The angular distribution of ρ° decay are to be analysed in three reference systems, the Gottfried-Jackson system, the Helicity system and the Adair system, which differ each in its choice of the spin quantization axis(Z-axis).

(i) The Gottfried-Jackson frame: the Z-axis is the direction of incident photon in the ρ° rest system.

(ii) The Helicity frame; the Z-axis is the direction of the ρ° in the overall (γ + P) c.m. system. i.e. opposite to the outgoing proton in the ρ° rest system.

(iii) The Adair frame: the Z-axis is taken along the direction of the incident photon in the overall (γ + P) c.m. system.

In all three systems, the Y-axis is always taken to be normal to the production plane, and for the ρ° meson produced forward, all three system concide. Depending upon its production mechanism in the reaction (25), the ρ° may be aligned in one of these three systems. In another word helicity conservation can be well seen in the specific channel for the corresponding proper frame. Namely (1) the G-J frame for t-channel helicity conservation, (2) the Helicity system for the s-channel c.m. system helicity conservation. (3) the Adair system for "spin independence" in the s-channel c.m. system.[14),21)] Our problem is then to find the density matrix elements of the ρ° decay and to determine the prefered system for describing ρ° production. Since detailed description of spin density matrix elements is given in my lecture at Sugadaira summer school,[2)] I should like to refer you to that or to Ref. 16).

Now the decay angular distribution in all three systems by linearly polarized photons can be expressed in terms of independent measurable spin density matrix, ρ_{ik}^{α} (here α refers to the polarization of incident photons. $\alpha = 0$ means unpolarized beam and the case of $\alpha \neq 0$ are for linearly polarized beam);

$$W(\cos\theta, \psi, \Phi) = \frac{3}{4\pi}\left\{\frac{1}{2}(1 - \rho_{00}^{0}) + \frac{1}{2}(3\rho_{00}^{0} - 1)\cos^2\theta\right.$$

$$-\sqrt{2}\, R_e\rho_{10}^{0}\sin2\theta\cdot\cos\psi - \rho_{1-1}^{0}\sin^2\theta\cos2\psi$$

$$-P_\gamma\cos2\Phi(\rho_{11}^{1}\sin^2\theta + \rho_{00}^{1}\cos^2\theta - \sqrt{2}\, R_e\rho_{10}^{1}$$

$$\sin2\theta\cos\psi - \rho_{1-1}^{1}\sin^2\theta\cos2\psi\,)$$

$$\left.-P_\gamma\sin2\Phi[\sqrt{2}\, I_m\rho_{10}^{2}\sin2\theta\cdot\sin\psi + I_m\rho_{1-1}^{2}\right.$$

$$\left.\sin^2\theta\sin2\psi\,]\right\} \qquad \cdots\cdots\cdots\cdots\cdots (29)$$

Here, P_γ is the degree of linear polarization of the photon; Φ is the angle of the photon electric polarization vector with respect to the production plane measured in the overall $(\gamma + P)$ c.m. system; θ and ψ are the polar and azimuthal angle of the π^+ in the ρ° rest frame. Fig. 15 shows relation of these angles. Looking at the density matrix elements in Fig. 17, we observe that in the helicity system, no helicity-flip term is significantly different from zero for the region of $|t| < 0.4$ GeV^2. This means there is no significant helicity-flip at the γ-ρ vertex. Accordingly we may summarize their experimental observation with a conclusion that the diffractively produced ρ° is consistent with conservation of the s-channel helicity of the photon. Since there is an incident that s-channel helicity seems to be conserved in πp elastic scattering[22], factorization suggests that Pomeranchuk exchange may be helicity conserving[16],[22] in, at least, the elastic scattering process.

Another analysis the SLAC-Berkeley collaboration made is concerned on the point of low mass skewing in the $\pi^+\pi^-$ mass shape at ρ°. Since this analysis is quite model-dependent, I whould rather prefer to leave the discussion on this point for your later reference. Instead, I would like to make one comment on the $\pi^+\pi^-$ mass distribution at higher energy region, where they have not seen any significant peak. This means no higher energy vector meson which decays predominantly to the $\pi^+\pi^-$ pair system. In connection with this conclusion, this group has very recently reported in their preliminary analysis of the 9.3 GeV 5-prong data that they have observed 4-pion state around 1600 MeV with possibly a vector character in the diffraction-like process[23].
It may be too early to say anything very definite on how to understand these observations.

§ 3-3 Longitudinal Phase Space Plot and the Prism Plot

As was discussed in § 2, there are so many hadron reactions which proceed through the production of strongly decaying resonances. So-called quasi-tow body reactions in which at least one out of two outgoing particles is a resonance, are very important in the study of hadron physics in the sense that the process can be understood very similarly to a typical elastic or simple exchange process. It is unfortunately not true that the process is always

to be simple. On the contrary situations are usually much complicated. For instance, reactions such as $\pi^+p \rightarrow \Delta^{++}\pi^0$ and $\pi^+p \rightarrow \rho^+p$ can not, in general, be distinguished by simply examining the three-body final state $\pi^+p \rightarrow \pi^+\pi^0p$. These two quasi-two body reactions are different and we have usually to examine each by itself separately from all other reactions that make the three particle final state of $p\pi^+\pi^0$.

In bubble chamber film analysis it is , in principle, possible that all the kinematical information such as four vectors $p(E, \vec{P})$ of each of the final state of the event are known. By using these kinematical information we hope to determine what sort of interactions occurred among these particles and what kind of resonances are produced.

Recently study of many-particle final state has become very fashionable, because of the developments of theories in connection with inclusive reactions, and of experimental techniques to analyse and present the data. Besides, it might be nice to recall that the many body final states occupy most of processes involved in high energy reactions, about 70 to 80 percents of the total cross section around 10 GeV/c. Difficulties are always there, when experimental physicists try to extract some physics from the data of many body reactions. That is how to draw a background to measure a significant physical effect in the data. It is in this connection, some trials have been tried to analyse the data. Longitudinal phase space plot developed by Van Hove[24] and the so-called Prism Plot developed by I, Pless and his collaborators[25] subsequently, are among others quite interesting and promissing. Here I will give a brief introduction to their concepts and the practical examples.

Historically it has long been known that in high energy collisions the transverse momentum P_T is approximately constant ($\sim$400 MeV/c) for all outgoing particles. It has also been found that one of the most sensitive varialbes to the reaction mechanism is the c.m. longitudinal momentum P_L^*.
The longitudinal phase space (LPS) analysis by Van Hove starts with understanding of these well known facts. The LPS analysis can be explained in terms of the plot shown in Fig. 18 for such three body reactions as

$$\pi^\pm p \longrightarrow p\pi^\pm\pi^0 \qquad \cdots\cdots\cdots\cdots (30)$$

The three variables plotted are the c.m. longitudinal momentum of the three

secondary particles, $P^*(p)$, $P^*(\pi^\pm)$ and $P^*(\pi^\circ)$. The three axis are inclined to one another at 120°. Accordingly for each event there is a unique point on the LPS plot. This is the very important feature of the LPS plot, since in the scattered plot of the event we can see a particle behavior in connection with other's in the plot. This is nothing else but most important dynamical correlation between particles envolved. Example of the experimental distribution of events in the LPS analysis are shown in Fig. 19 for the reaction $\pi^- p \to p\pi^-\pi^\circ$ at 16 GeV/c[26]. It may be seen that experimental points all lie near the boundary of the LPS plot. This is because the transverse momenta of all three particles is small. This fact allows us to convert this two-dimensional LPS plot into a simpler one-dimensional distribution.

This is done by introducing a sensitive angular variable ω, measured anticlockwise from the axis of $P^*(\pi^\pm) = 0$ as is shown in Fig. 19. This polar angle ω is sometimes called as a Van Hove angle. By using the ω-variable, we may be able to separate the events with different reaction mechanism as peak in the ω-angular distribution. Bialas et al[27] have first shown by using this technique that whenever possible the diffraction mechanism dominates three body reactions at high energy. Applications of the method to various reactions are now being tried[26),28].

One of the most interesting and promising extention of the Van Hove LPS analysis is the Prism Plot developed by I. Pless and his collaborators[25]. Essential point of their idea in making a Prism Plot analysis is based on the use of the Van Hove angle ω in addition to other variables. For three body final state at a given condition with unpolarized beam and target, there are only four variables required to completely specify the final state. In their Prism Plot analysis of the reaction $\pi^+ p \to p\pi^+\pi^\circ$ at 3.9 GeV/c, Pless et al[25] used this Van Hove angle ω together with the total energies of the outgoing proton and one of the pions. The fourth variable they used is the ratio R/Rmax, of the length of the radial vector (R) in the Van Hove plot to the maximum length (Rmax) that vector could have at the given Van Hove angle (See Fig. 18 and Fig. 20). Two energy variables can best be represented by a point in an energy equilateral triangle, namely in the Dalilz plot. If we use the Van Hove angle ω as a z-coordinate together with the two dimensional energy simplex, we construct a data plot bounded by a rectangular

equilateral prism. The outline of such a prism is shown in Fig. 20, which illustrates the reason for calling the method Prism Plot analysis. When we utilize the variable R/Rmax, analysis gives much better insight, in separating the events comming from different mechanism. Fig. 21 shows the example how the R/Rmax-distribution relates to the Prism Plot. Fig. 21 (a) and (b), which are Monte Carlo data for the Lorentz invariant phase space, have a difuse set of point in the Prism Plot and R/Rmax is symmetric about 0.5 and has a peak at the centre. In contrast, Fig. 21 (c) and (d), which are their $\pi^+p \rightarrow \pi^+\pi^+\pi^0 p$ data at 3.9 GeV/c, show that the events cluster into three sharp tubes and R/Rmax peaks at around 0.9. Comparing Fig. 21 (b) and (d), one sees immediately that so-called Lorentz invariant phase space plays almost no role in this final state. This clustering into three sharp tubes seems to be due to dynamical reasoning. Namely, it has been shown that each tube contains a resonance produced, or any two-body correlation between the particles. The clustering is also a reflection of such dynamical properties of many body reactions as the limitted transverse momentum, P_T and the correlation between particles and resonances produced.

Three body final state produced in the π^+p reaction can be any of the following;

$$\pi^+ + p \longrightarrow \Delta^{++} + \pi^0$$
$$\longrightarrow \Delta^+ + \pi^-$$
$$\longrightarrow p + \rho^+$$
$$\longrightarrow (p\pi^0) + \pi^+ \quad \text{(diffraction dissociation)}$$
$$\longrightarrow p + \pi^+ + \pi^0 \quad \text{(pure phase space)}$$

In their analysis with the Prism Plot, I. Pless et al showed with remarkable success that events in each tube well correspond to the events which form a resonance or two-body correlation produced in either of the reactions listed above. Fig. 22 (b) is the (π^+p) invariant mass distribution for the events in the upper tube in the Prism Plot and Fig. 22 (d) the ($\pi^+\pi^0$) mass distribtuion for the central tube of the Prism Plot. Corresponding (π^+p) and ($\pi^+\pi^0$) invariant mass distributions for the total samples are given in Fig. 22 (a) and (c), respectively. One sees very clearly that Δ^{++}

and ρ^+ productions dominate the process in each case. The authors stressed that the diffraction dissociation is contained in the lower tube of the plot together with the Δ^+ production. From this result, we may say that "wrong pairing" of the particles shows no resonances and smear out the true resonant peak, although the Lorentz phase space has nothing to do with this smearing.

Since it is usually very difficult to extract events of a specific production mechanism from all the other events envolved in the reaction, it seems to me quite remarkable that this selection of the clustered events in the Prism Plot could be done without any sacrifice of universality of its selection criteria, or in another word, without any particular biases. Although the method looks promissing, there seems to be much to be done before we conclude its very usefulness in the study of many body reactions. As they discussed in their paper[25], the technique can easily be generalized to the four-body final state also. I would, however, like to leave this problem for you.

§4. Aknowledgement

I wish to thank Professor H. Sugawara and Dr. T. Sato for their enlightning discussions. I also thank Professor Y. Hara for reading this note and for making helpful suggestions.

References

1) CERN THRESH-GRIND Program Manual

2) K. Takahashi, Determination of spin and parity for resonances SJC-P-66-8 (1966) Page 125.

3) G. Chew and F. Low; Phys. rev. 113 (1959) 1640.

4) G. Wolf; Phys. Rev. 182, (1969) 1538.

5) E. Colton et al; UCLA-Report, UCLA-1027 (1968) unpublished and E. Colton et al; Phys. Rev. D3 (1971) 1063.

6) J. L. Petersen, Physics Reports 2C (1971) 157. For recent individual works, see for example L. Chen and V. Hagopian, Physical Rev. D2 (1970) 583 and E. Colton et al. Phys. Rev. D3 (1971) 2033.

7) K. Takahashi et al; Phys. Rev. D6 (1972) 1266 and the paper presented at the US-Japan Joint Seminar on Elementary Particle Physics with Bubble chamber Detectors. March 1971, SLAC-Report No. 144 (1972).

8) For Example P.K. Wiliams, Phys. Rev. D1 (1970) 1312.

9) M. Alston-Garnjost et al; Phys. Letters 36B (1971) 152, S.M. Flatte et al; Phys. Letters 38B (1972) 232 and S.D. Protopopescu et al; Lawrence Berkeley Lab. Univ. of California, LBL-787 (1972).

10) H.P. Dürr and H. Pilkuhn; Nuovo Cimento 40A (1965) 899.

11) T. Sato; PhD Thesis of Tohoku University. 1971 (unpublished).

12) A.A. Carter et al; Nuclear Phys. B26 (1971) 445.

13) Y. Fujii and M. Kato, University of Tokyo. College of General Education preprint, 1972 (unpublished) and Y. Fujii, Phys. Letters 39B (1972) 179.

14) J. Ballam et al; Phys. Rev. Letters. 24 (1970) 960, 24(1970) 1467(E), 24 (1970) 1364, H. H. Bingham et al, Phys. Rev. Letters. 24 (1970) 955, 25 (1970) 1223.

15) G. Chadwick; Paper presented at the US-Japan Joint Seminar on Elementary Particle Physics with Bubble Chamber Detectors, March 1971, SLAC-Report No. 144 (1972).

16) J. Ballam et al; Phys. Rev. D5 (1972) 545.

17) J. Beaupre et al; Phys. Letters 34B (1971) 160, G. Ascoli et al; Phys. Rev. Letters 26 (1971) 929 and G. Ascoli, a talk given at the Third International Conference on Experimental Meson Spectroscopy held at University of Pennsylvania, April (1971, unpublished) 28-29.

18) K. Takahashi; Recent Developments in Inclusive Experiments, (in Japanese) Bulletine of Phys. Society of Japan, Vol. 27 (1972) 489.

19) R. L. Thews; Phys. Rev. 175 (1968) 1749.

20) K. Schilling, P. Seyboth and G. Wolf, Nuclear Phys. B15 397, B18 332 (E) (1970).

21) Y. Eisenberg et al; Phys. Letters 22 (1966) 223.

22) F. J. Gilman et al; Phys. Letters 31B (1970) 387.

23) SLAC-LBL collaboration presented at the 3rd International Conference on Experimental Meson Spectroscopy, University of Pennsylvania, Philadelphia, April 1972, and G. Smadja et al, LBL-991 (1972, unpublished).

24) L. Van Hove; Phys. Letters 28B (1969) 429 and Nuclear Physics B9 (1969) 331.

25) J. E. Brau et al; Phys. Rev. Letters 27 (1972) 1481.

26) Bartsch et al (Auchen-Berlin-Bonn-CERN-Cracow-Heidelberg-Warsaw collaboration) Nuclear Physics B19 (1970) 381 and D. R. O. Morrison "Review of strong interactions of kaons", CERN/D. PH. II/PHYS 69-28 (1969, unpublished).

27) A. Bialas et al; Nuclear Physics B11 (1969) 479.

28) J. Beaupre et al; Nuclear Physics B35 (1971) 61

Figure captions

Fig. 1. Dalitz plot for the reaction $\pi^- p \longrightarrow \pi^- \pi^+ n$ at 8 GeV/c.
Total 3567 events. Ref. 7) and 11).

Fig. 2. Chew-Low plot for $\pi^+\pi^-$ in the reaction $\pi^- p \longrightarrow \pi^- \pi^+ n$ at 8 GeV/c, 3567 events. Ref. 7) and 11).

Fig. 3. A Feynman diagram showing a one-pion-exchange (OPE) mechanism.

Fig. 4. Differential cross sections $d\sigma/d|t|$ for events of the reaction $pp \rightarrow \Delta^{++} n$ in the Δ^{++} region ((a) and (b) on the left) and for the events of the reaction $\pi^+ p \rightarrow \Delta^{++} \rho^0$ in the $\Delta^{++} - \rho^0$ region ((a)-(d) on the right). The solid curves give the results of the OPE fit.

Fig. 5. Examples of comparisons of calculated on-mass-shell cross sections by using corresponding reactions (reaction (4) and (4)', for example) with the measured on-mass-shell cross sections.

Fig. 6. $d\sigma/dt$-distribution for $\pi^- p \longrightarrow \pi^- \pi^+ n$ reaction at 8GeV/c shows strong absorption effect (a), while the reaction $\pi^+ p \longrightarrow \pi^+ \pi^- \Delta^{++}$ has no such absorption effect (b). Figure (a) is from Ref. 7) and (b) from Ref. 9).

Fig. 7. A Feynman diagram showing a one-pion-exchange (OPE) mechanism in the reaction $\pi^+ p \rightarrow \pi^+ \pi^- \pi^+ p$.

Fig. 8. (a) $\pi^+ p$ mass distribution for $\pi^+ p \longrightarrow \pi^+ \pi^- \pi^+ p$ reaction at 7 GeV/c, both combination for π^+ included.
(b) $\pi^- \pi^+$ mass distribtuion in the same bin size (20 MeV), both combination included.
(c) $\pi^- \pi^+$ mass distribution in the same bin size, for the events with Δ^{++} selected.

Fig. 9. $\pi^+\pi^-$ cross sections ((a) is an extrapolated one) and K^+K^- cross section obtained in the 7 GeV/c $\pi^+ p \rightarrow \pi^+ \pi^- \Delta^{++}$ and $\pi^+ p \rightarrow K^+ K^- \Delta^{++}$ reactions.

Fig. 10-12. $\langle Y_L^0 \rangle$ moments for extrapolated data and for $|t'_{pA}| < 0.1$ Gev^2, for L = 1 ~ L = 6 (Ref. 9)).

Fig. 13. Extrapolated $\langle Y_1^0 \rangle$ moments for $\pi^+ p$ vertex. Solid curves correspond to physical $\pi^+ p$ scattering. (Ref. 9)).

Fig. 14. Dipion mass spectrum of reaction (26) obtained in the bubble chamber for E_γ = 9.3 GeV.

Fig. 15. Coordinate system illustrating the production of the reaction (26), the decay plane of ρ^0 and polarization vector of the incident photon, ε_γ in the ρ^0-rest system.

Fig. 16. Decay angular distribution of π^+ from ρ^0 in the ρ^0 rest frame, showing the natural parity exchange dominance in the ρ^0 photoproduction process.

Fig. 17. Density matrix elements of the ρ^0 decays in the G-J., the helicity, and the Adair systems.

Fig. 18. Principle of Van Hove hexagonal plot in the longitudinal phase space (LPS) analysis.

Fig. 19. An example of LPS analysis for the events of $\pi^- p \to p\pi^-\pi^0$ at 16 GeV/c (Ref. 23).

Fig. 20. Three body Van Hove plot, the triangular Dalitz plot and the principle of Prism Plot analysis.

Fig. 21. An example showing how the R/Rmax-distribution relates to the Prism Plot. (a) and (b) are for the Monte Carlo events for the Lorentz invariant phase space, and (b) and (d) are the same plot and distribution for the real events of $\pi^+ p \to p\pi^+\pi^0$ reaction at 3.9 GeV/c (Ref. 25).

Fig. 22. $(p\pi^+)$ and $(\pi^+\pi^0)$ invariant mass distributions for the events of

$\pi^+ p \rightarrow p\pi^+\pi^\circ$ reaction at 3.9 GeV/c. (a) and (b) are the distributions without any selection, and (c) and (d) are the corresponding mass distributions with the tagged Δ^{++} and the tagged ρ^+ events through the Prism Plot analysis. (Ref. 25).

9)

Table I Properties of two different fits.

Case	Description	Degrees of freedom	χ^2	S^* pole	ϵ pole
1	Background phase for $\ell \neq 0$ waves given by: $\delta_B^{(\ell)} = q^{2\ell+1} \sum_{n=0}^{N} a_n^{(\ell)} q^n$ M-matrix elements: $M_{ij} = M_{ij}^0 + M_{ij}^1 (s-s_0) + M_{ij}^2 (s-s_0)^2$ See text for complete description	147	152.2	980 ± 6 $-i(37 \pm 8)$ II sheet	600 ± 100 $-i(250 \pm 70)$ II sheet
2	Background phase for $\ell \neq 0$ waves given by: $\delta_B^{(\ell)} = q\, D_\ell(q) \sum_{n=0}^{N} a_n^{(\ell)} q^n$ M-matrix elements: $M_{ij} = M_{ij}^0 + M_{ij}^1 (E-E_0) + M_{ij}^2 (E-E_0)^3$ Otherwise same as case 1.	147	153.6	975 ± 6 $-i(39 \pm 8)$ II sheet	650 ± 70 $-(150 \pm 50)$ IV sheet

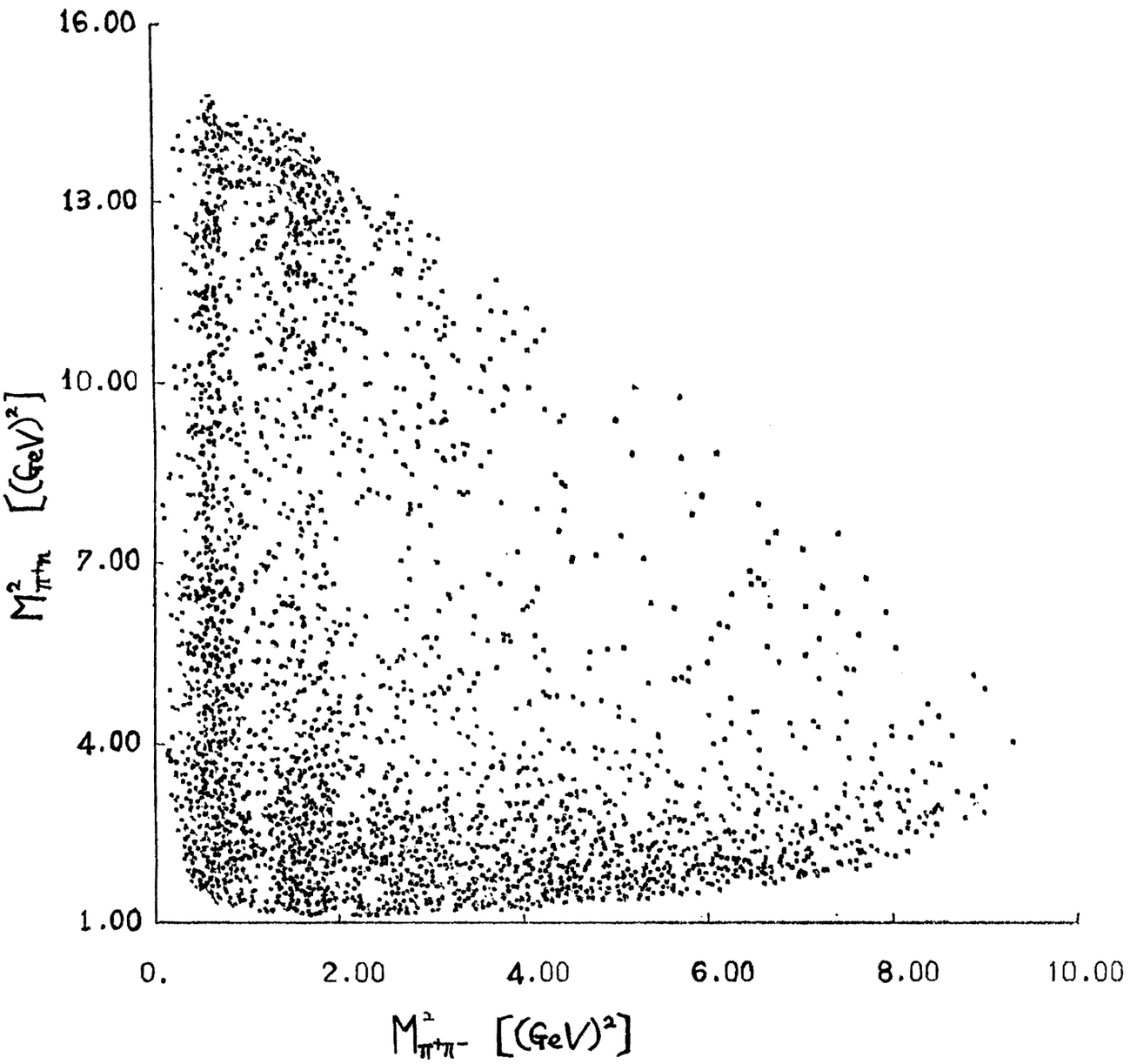
16.00
13.00
10.00
7.00
4.00
1.00
$M^2_{\pi^+\pi}$ [(GeV)^2]
0.
2.00
4.00
6.00
8.00
10.00
$M^2_{\pi^+\pi^-}$ [(GeV)^2]

Fig. 1

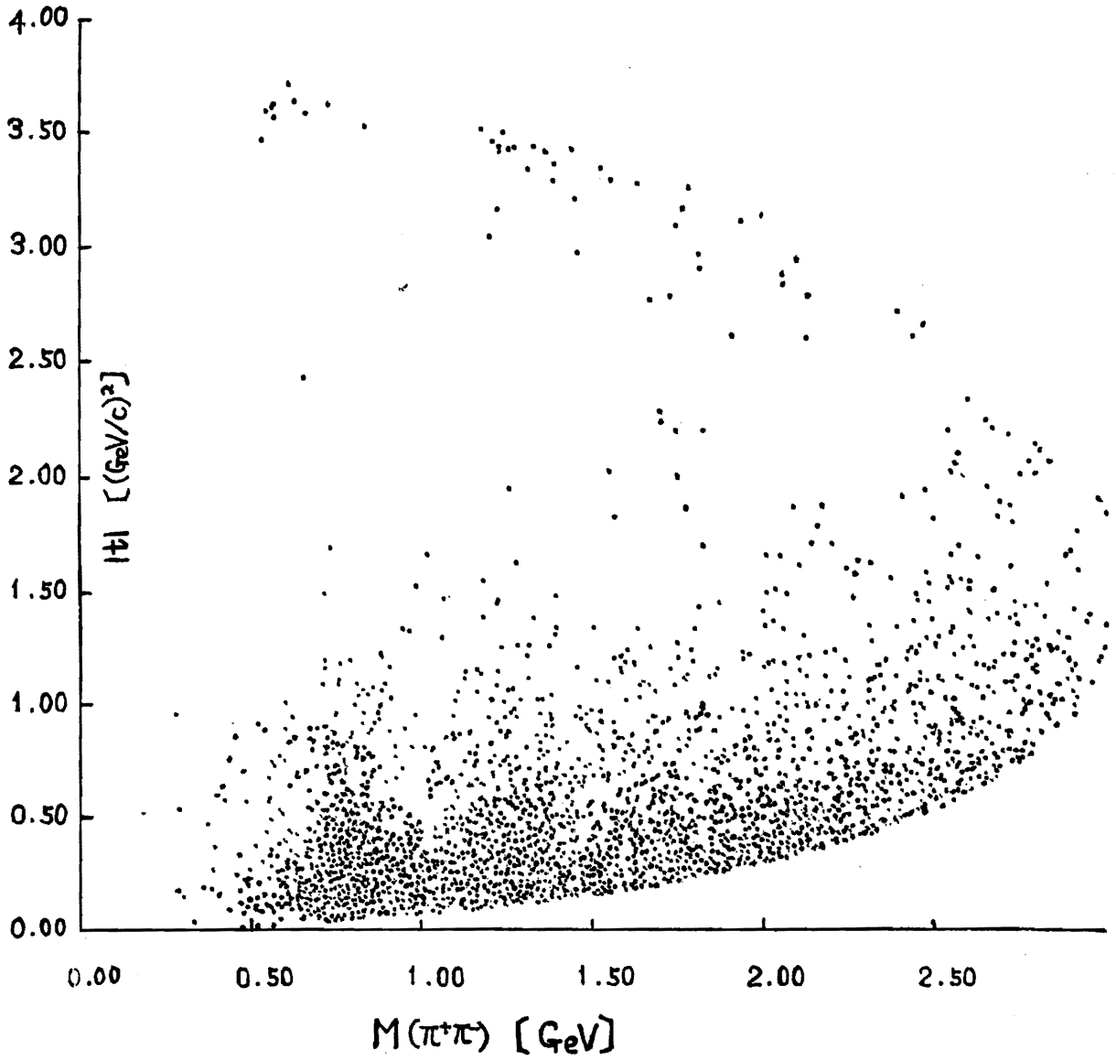
4.00
3.50
3.00
2.50
2.00
1.50
1.00
0.50
0.00
|t| [(GeV/c)²]
0.00
0.50
1.00
1.50
2.00
2.50
M(π⁺π⁻) [GeV]

Fig. 2

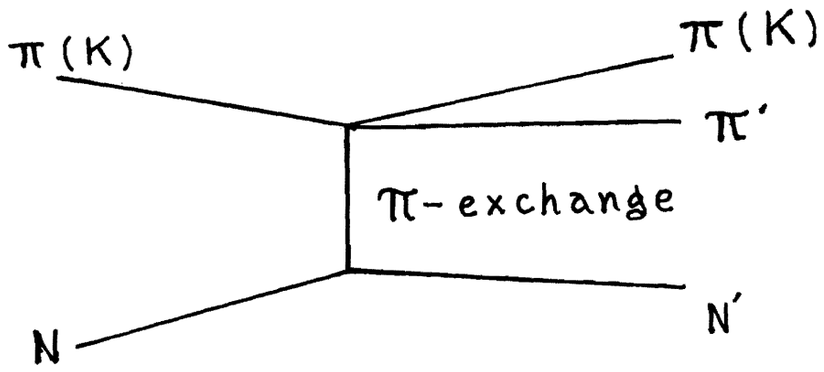
π (K)
π (K)
π'
π- exchange
N
N'

Fig. 3

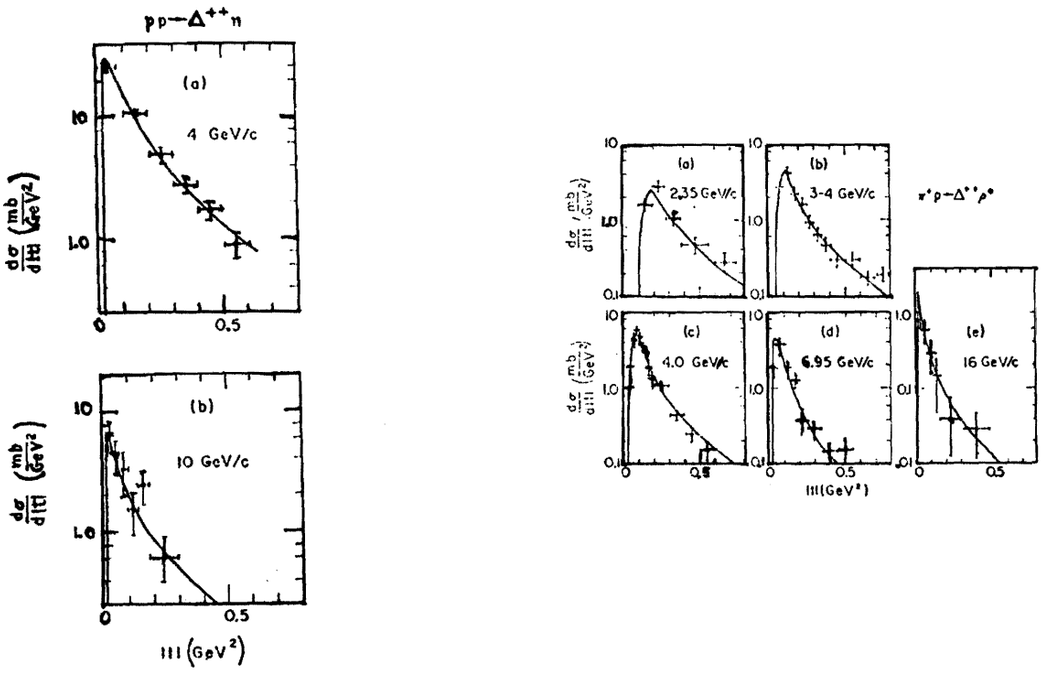
pp→Δ⁺⁺n
(a)
4 GeV/c
(b)
10 GeV/c
dσ/dt (mb/GeV²)
|t| (GeV²)
(a)
2.35 GeV/c
(b)
3-4 GeV/c
π⁺p→Δ⁺⁺ρ⁰
(c)
4.0 GeV/c
(d)
6.95 GeV/c
(e)
16 GeV/c
|t|(GeV²)

Fig. 4

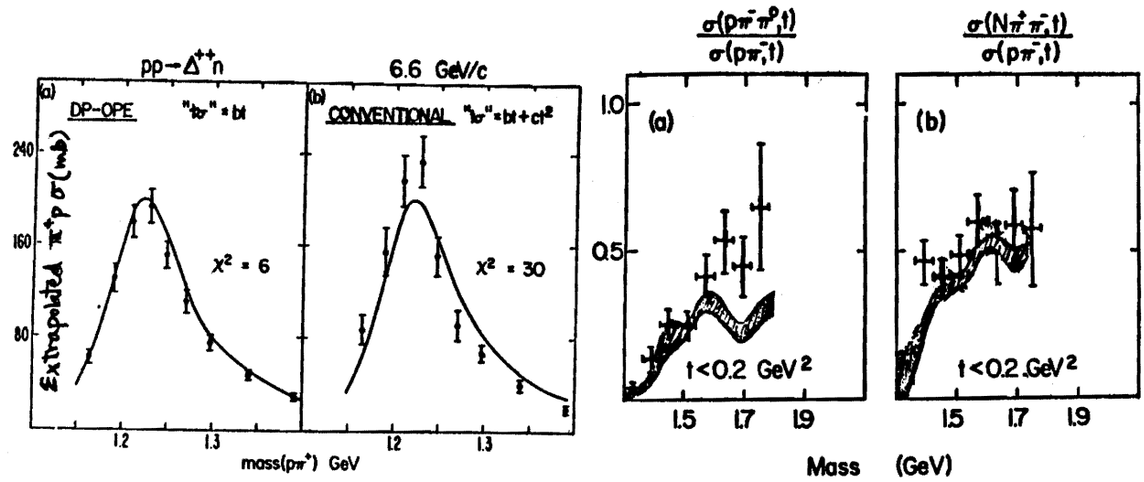
pp→Δ⁺⁺n
6.6 GeV/c
(a)
DP-OPE
"tσ" = bt
(b)
CONVENTIONAL
"tσ" = bt + ct²
Extrapolated π⁺p σ(mb)
240
160
80
χ² = 6
χ² = 30
1.2
1.3
mass(pπ⁺) GeV
σ(pπ⁻π⁰,t) / σ(pπ⁻,t)
σ(Nπ⁺π⁻,t) / σ(pπ⁻,t)
1.0
0.5
(a)
(b)
t<0.2 GeV²
t<0.2 GeV²
1.5
1.7
1.9
Mass (GeV)

Fig. 5

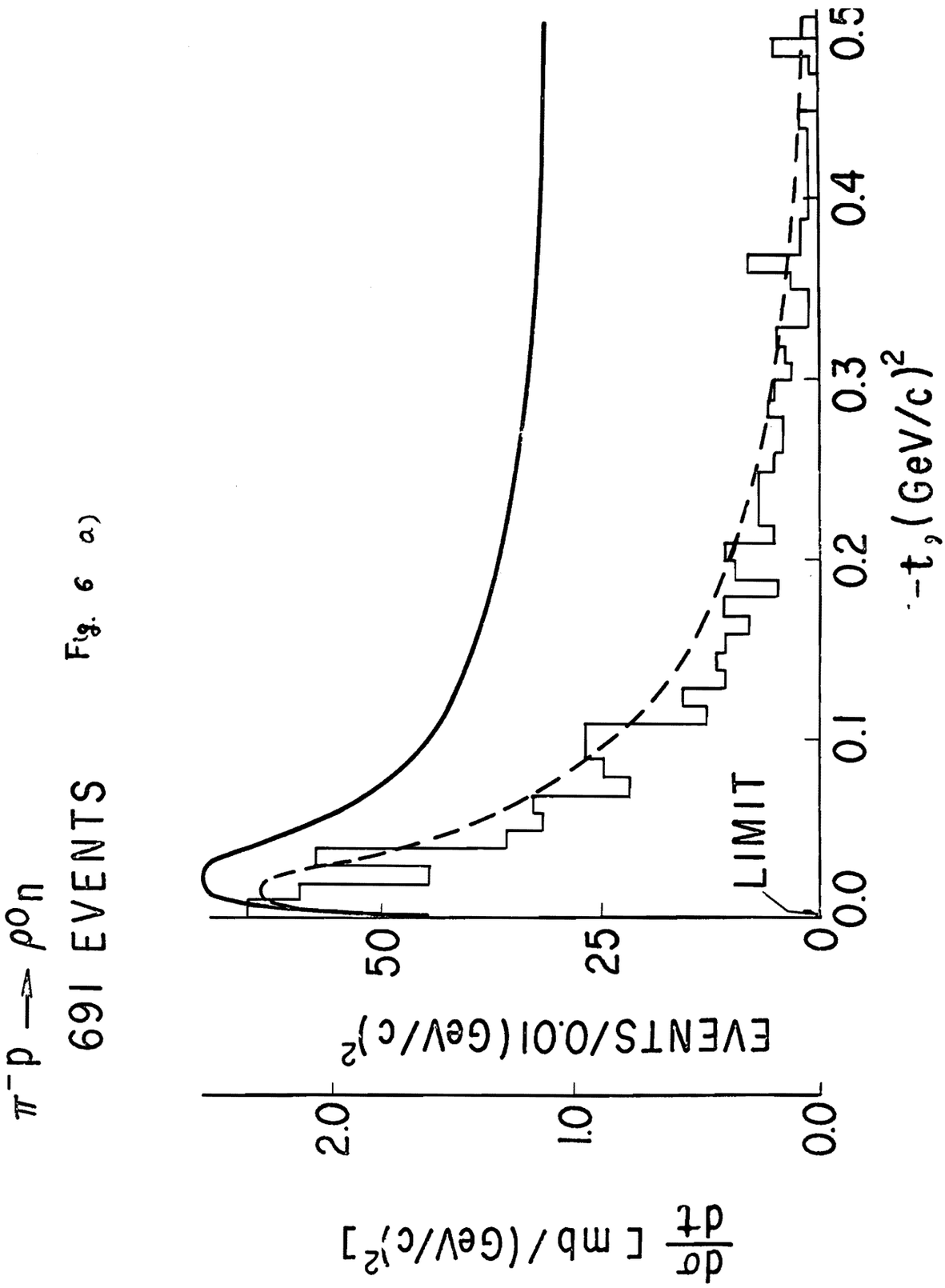
$\pi^- p \rightarrow \rho^0 n$
691 EVENTS
LIMIT
$\frac{d\sigma}{dt}$ [mb/(GeV/c)^2]
EVENTS/0.01(GeV/c)^2
$-t_\rho$(GeV/c)^2
0.0
0.1
0.2
0.3
0.4
0.5
25
50
1.0
2.0

Fig. 6 a)

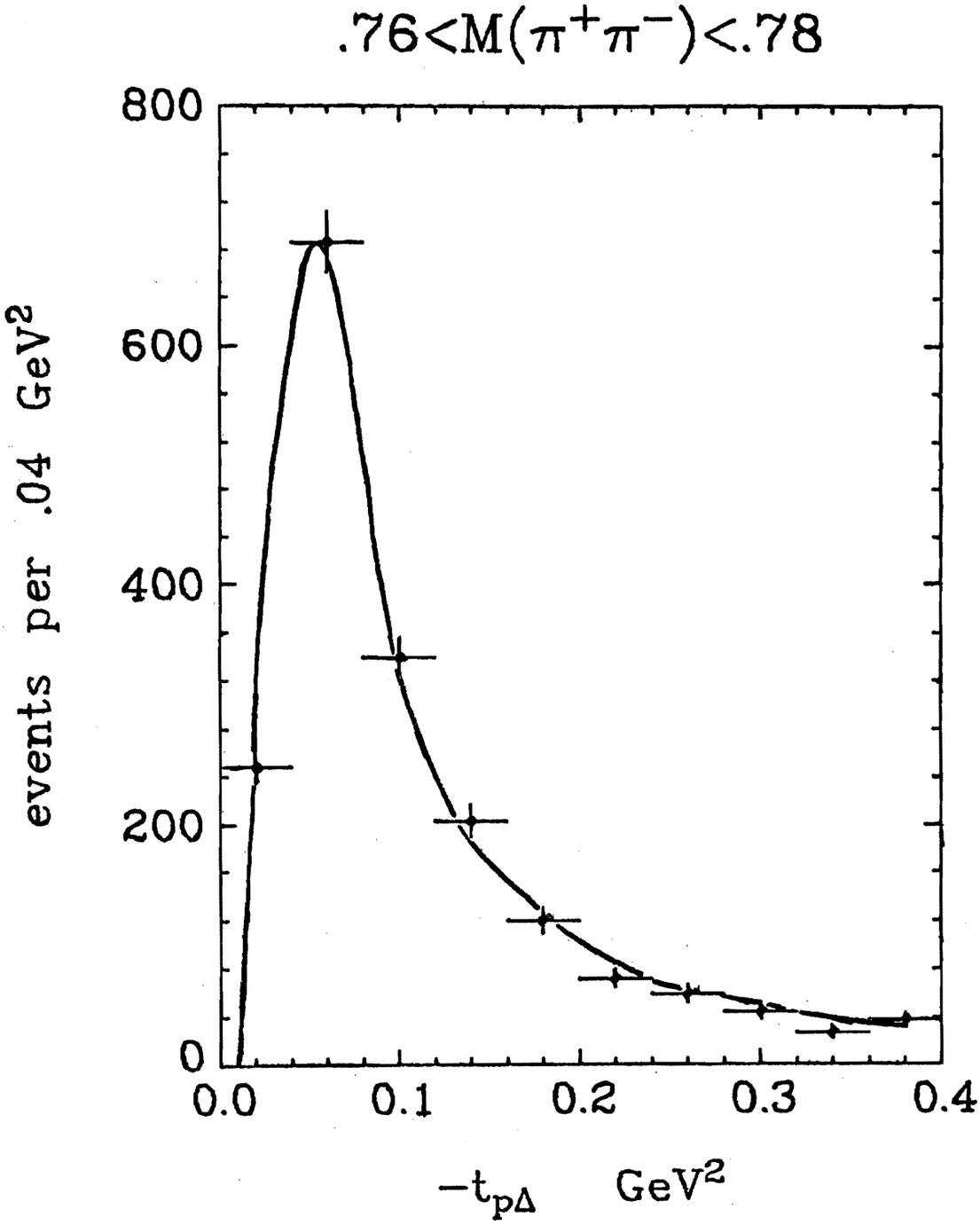
.76<M(π+π−)<.78
800
600
400
200
0
events per .04 GeV2
0.0
0.1
0.2
0.3
0.4
−tpΔ GeV2

Fig. 6 b)

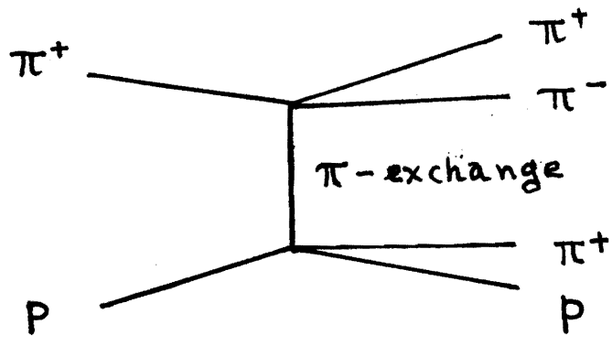
π+
π+
π−
π - exchange
π+
P
P

Fig. 7

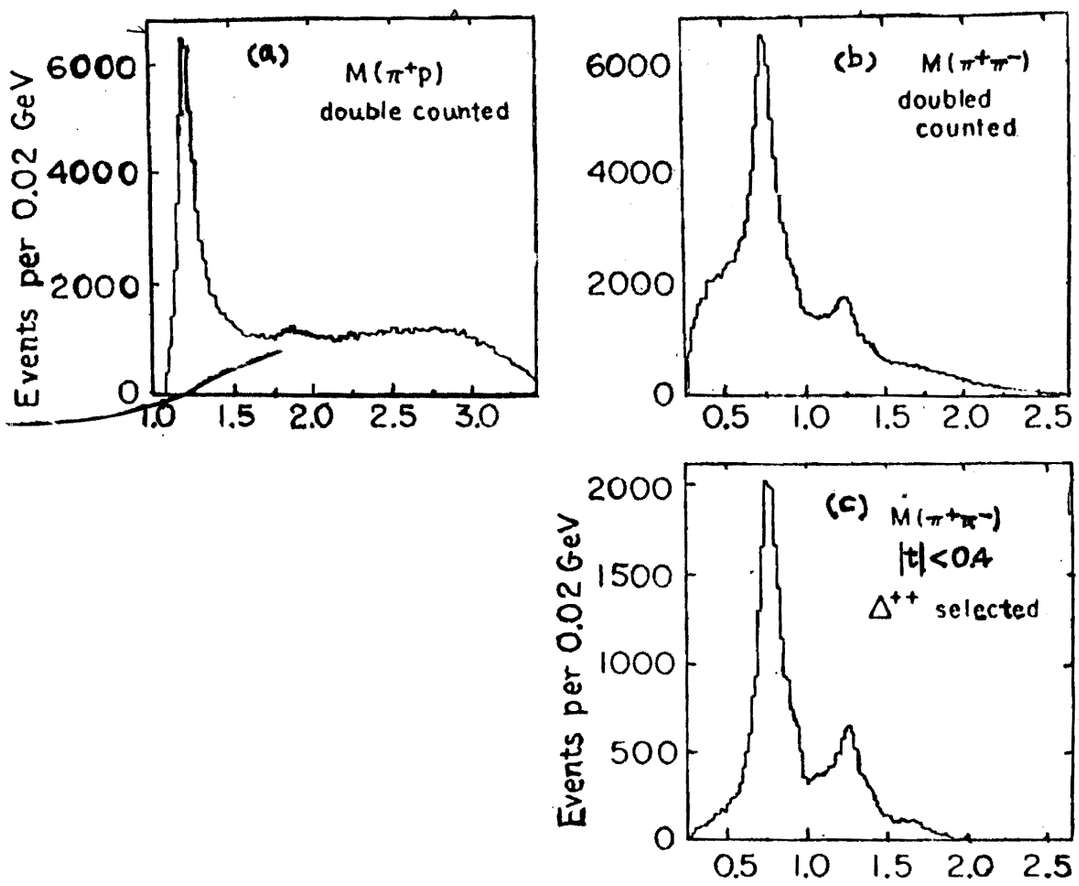
(a)
M(π+p)
double counted
Events per 0.02 GeV
6000
4000
2000
0
1.0
1.5
2.0
2.5
3.0
(b)
M(π+π−)
doubled
counted
6000
4000
2000
0
0.5
1.0
1.5
2.0
2.5
(c)
M(π+π−)
|t|<0.4
Δ++ selected
Events per 0.02 GeV
2000
1500
1000
500
0
0.5
1.0
1.5
2.0
2.5

Fig. 8

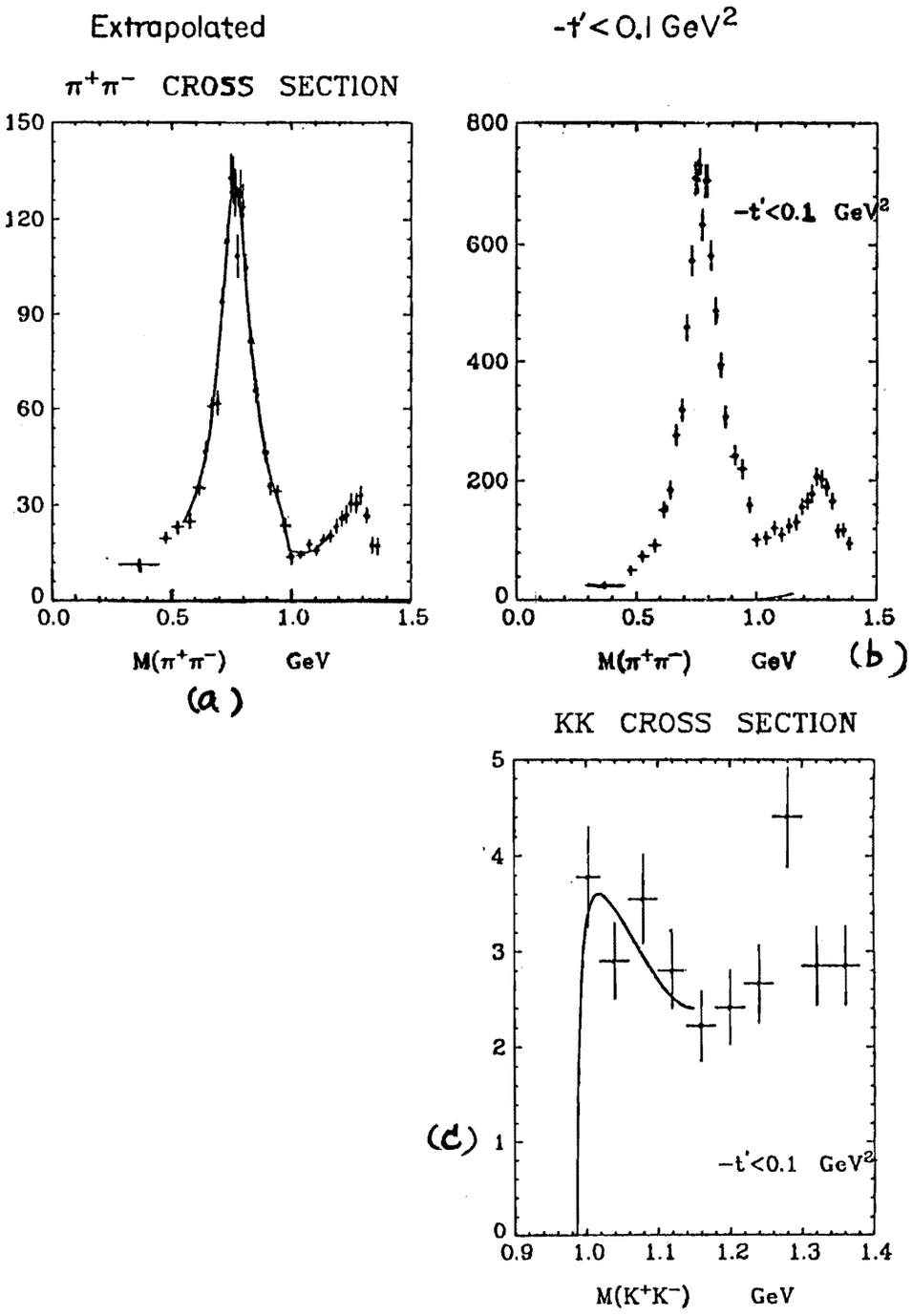
Extrapolated
$\pi^+\pi^-$ CROSS SECTION
150
120
90
60
30
0
0.0
0.5
1.0
1.5
M($\pi^+\pi^-$) GeV
(a)
$-t' < 0.1$ GeV^2
800
600
400
200
0
$-t'<0.1$ GeV^2
M($\pi^+\pi^-$) GeV
(b)
KK CROSS SECTION
5
4
3
2
1
0
(c)
$-t'<0.1$ GeV^2
0.9
1.0
1.1
1.2
1.3
1.4
M(K^+K^-) GeV

Fig. 9

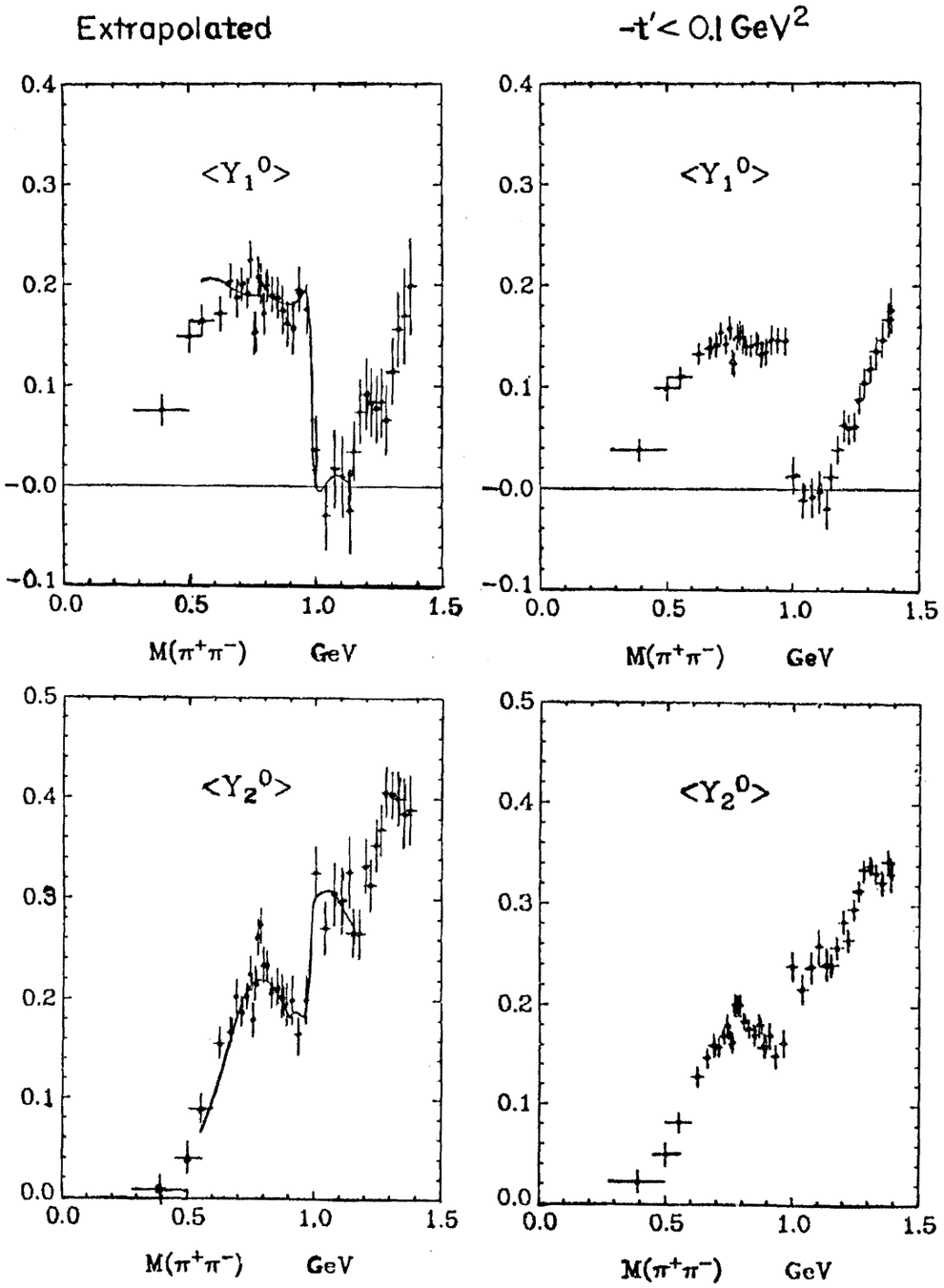
Extrapolated
$-t' < 0.1\ GeV^2$
$\langle Y_1^0 \rangle$
$\langle Y_2^0 \rangle$
$M(\pi^+\pi^-)$ GeV

Fig. 10

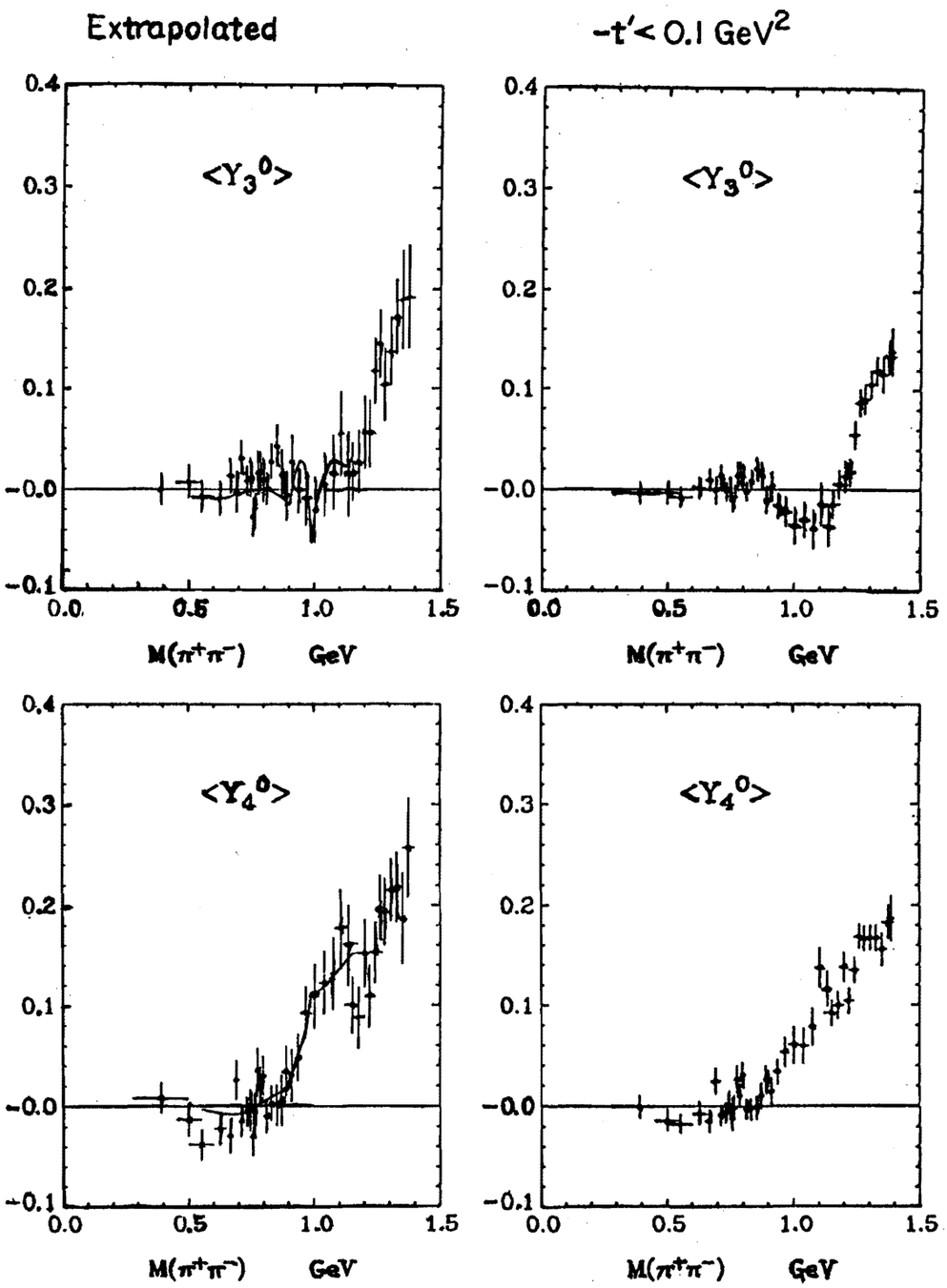
Extrapolated
$-t' < 0.1$ GeV^2
$\langle Y_3^0 \rangle$
$\langle Y_4^0 \rangle$
0.4
0.3
0.2
0.1
-0.0
-0.1
0.0
0.5
1.0
1.5
$M(\pi^+\pi^-)$ GeV

Fig. 11

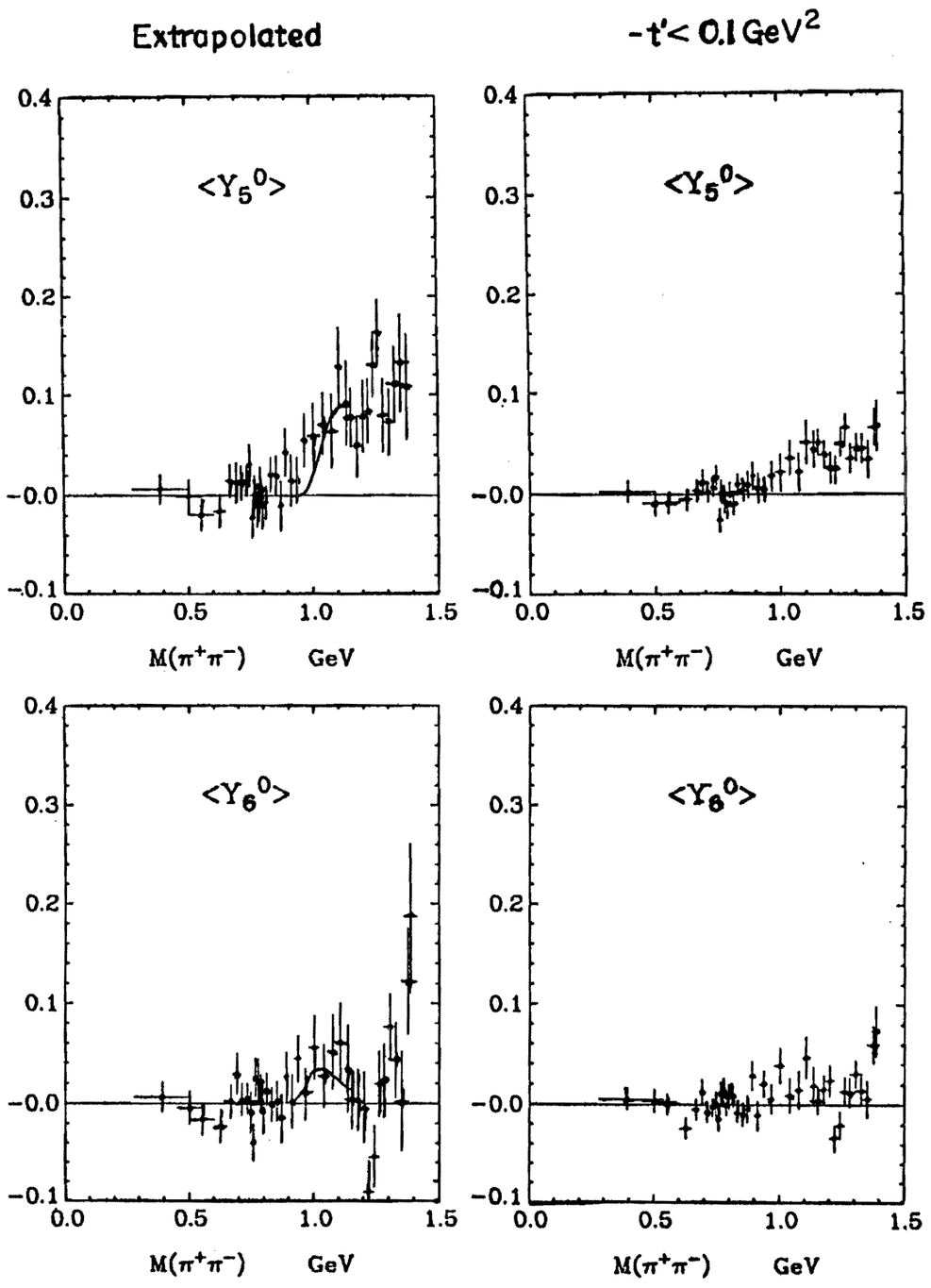
Extrapolated
$-t' < 0.1\ GeV^2$
$\langle Y_5^0 \rangle$
$\langle Y_5^0 \rangle$
$\langle Y_6^0 \rangle$
$\langle Y_6^0 \rangle$
0.4
0.3
0.2
0.1
-0.0
-0.1
0.0
0.5
1.0
1.5
$M(\pi^+\pi^-)$ GeV

Fig. 12

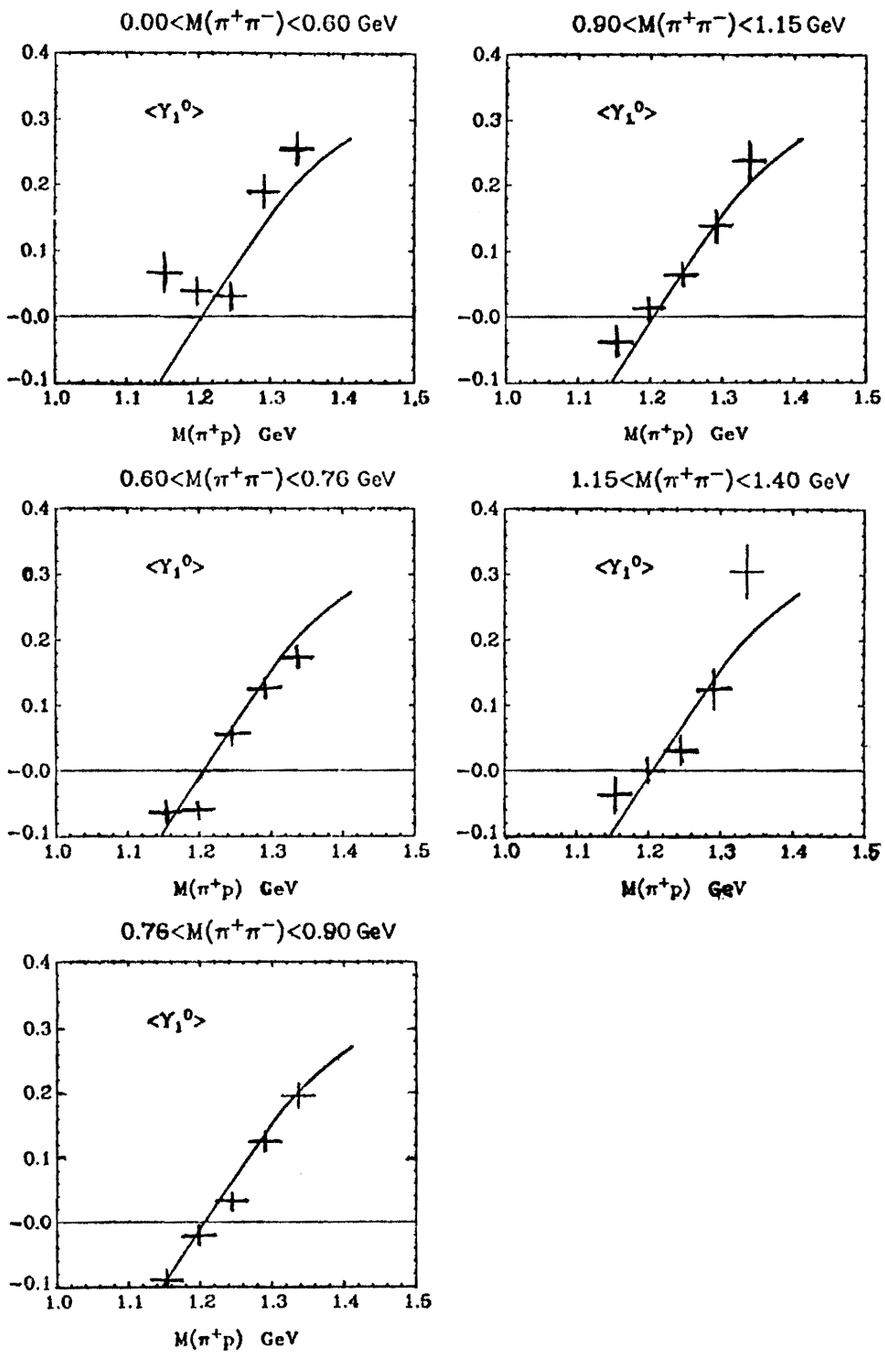
0.00<M(π+π−)<0.60 GeV
0.90<M(π+π−)<1.15 GeV
0.60<M(π+π−)<0.76 GeV
1.15<M(π+π−)<1.40 GeV
0.76<M(π+π−)<0.90 GeV
<Y1⁰>
M(π+p) GeV

Fig. 13

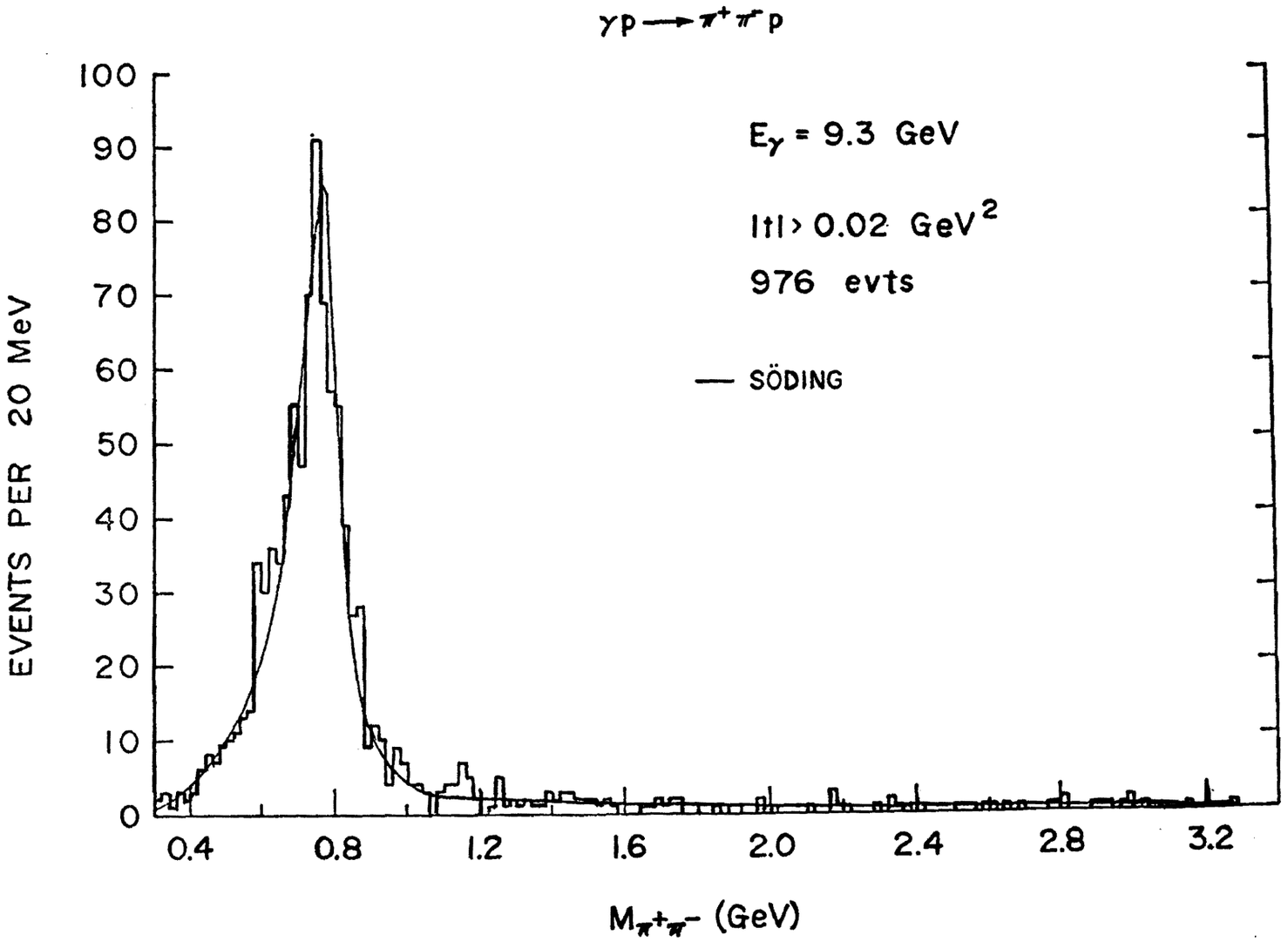
γp → π⁺π⁻p
E_γ = 9.3 GeV
|t| > 0.02 GeV²
976 evts
— SÖDING
EVENTS PER 20 MeV
100
90
80
70
60
50
40
30
20
10
0
0.4
0.8
1.2
1.6
2.0
2.4
2.8
3.2
$M_{\pi^+\pi^-}$ (GeV)

Fig. 14

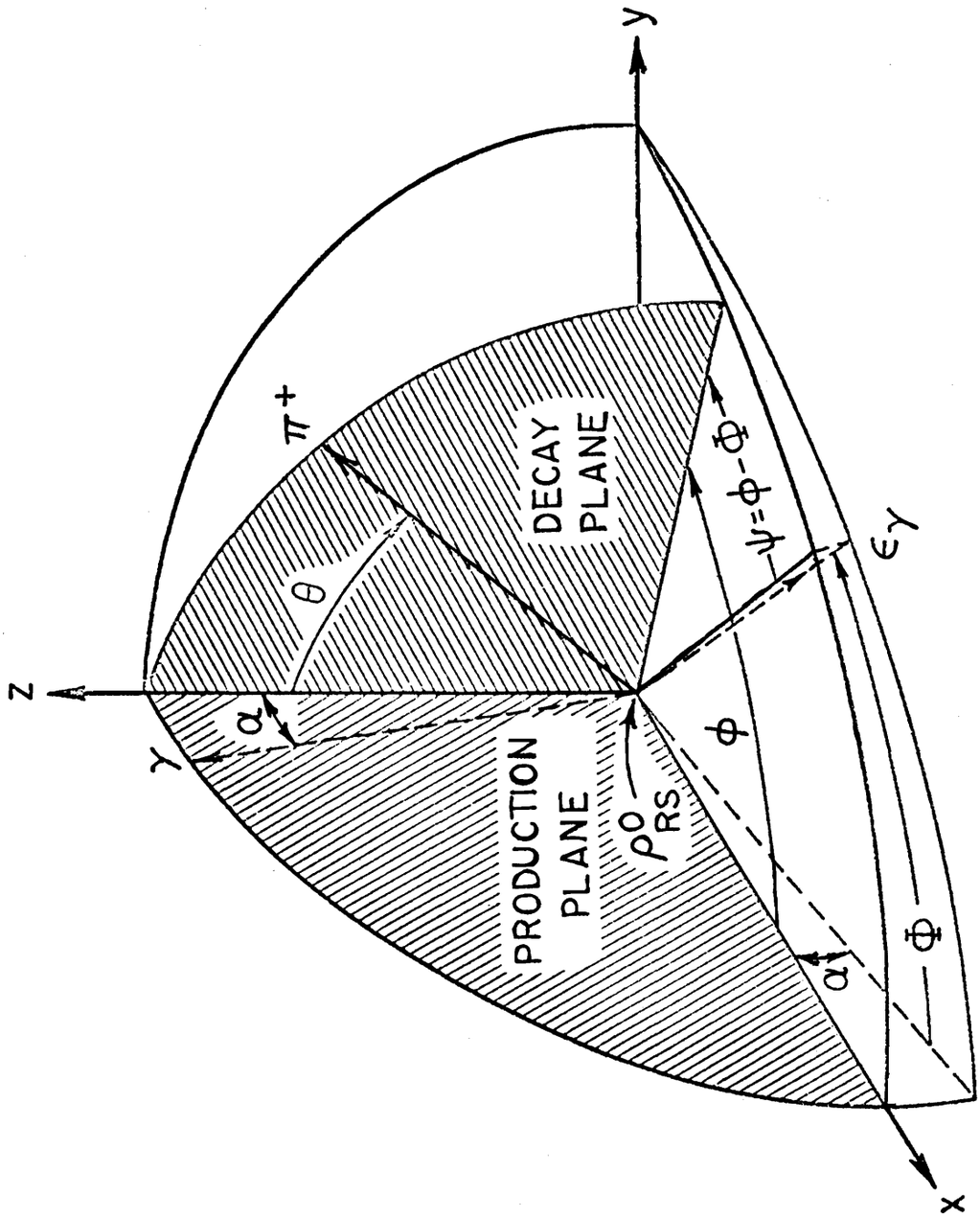
y
z
x
π^+
θ
DECAY PLANE
$\psi=\phi-\Phi$
$\epsilon\gamma$
α
γ
PRODUCTION PLANE
ρ^0_{RS}
ϕ
α'
Φ

Fig. 15

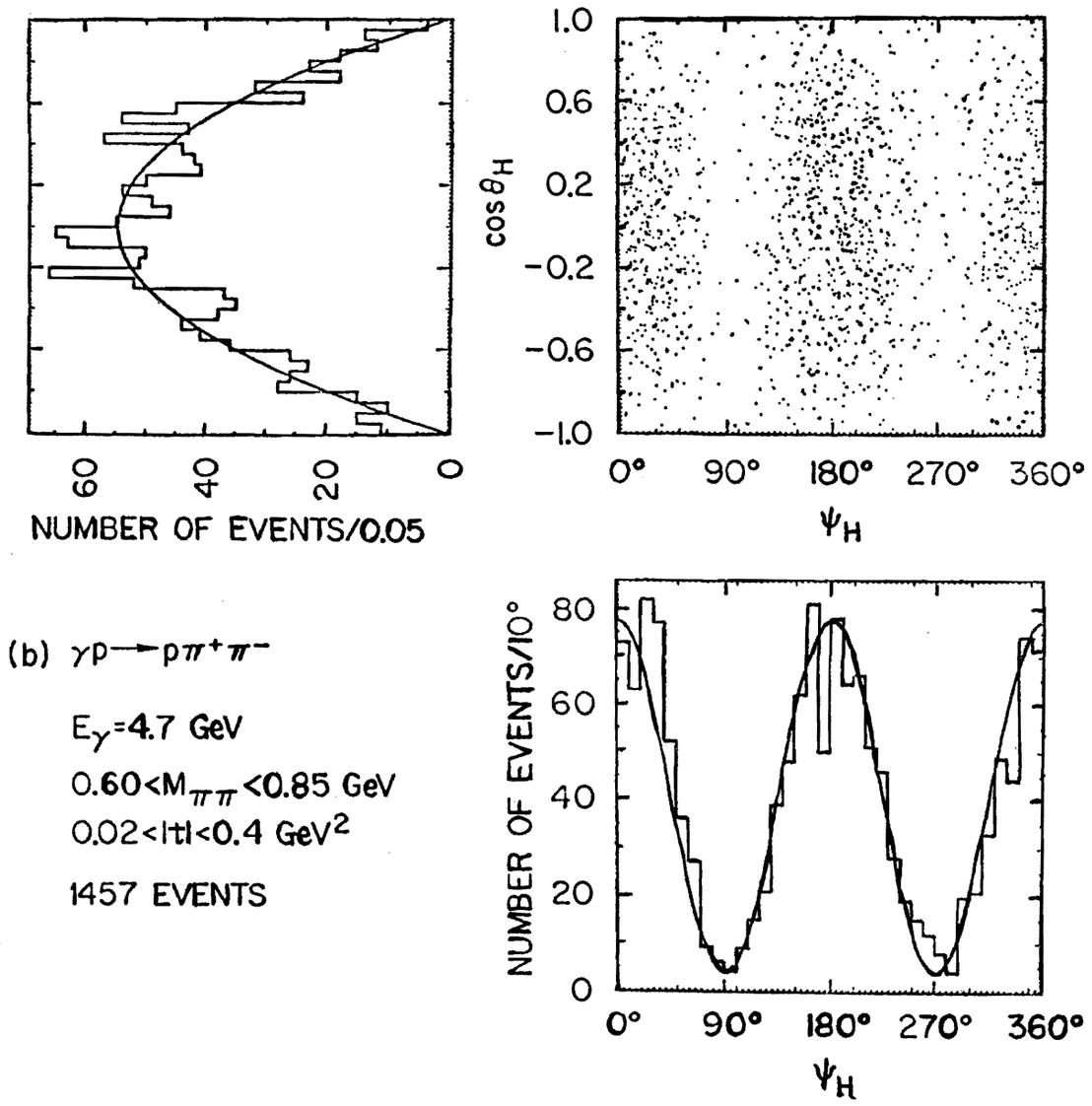
60
40
20
0
NUMBER OF EVENTS/0.05
1.0
0.6
0.2
-0.2
-0.6
-1.0
cos θH
0°
90°
180°
270°
360°
ΨH
(b) γp→pπ+π−
Eγ=4.7 GeV
0.60<Mππ<0.85 GeV
0.02<|t|<0.4 GeV2
1457 EVENTS
NUMBER OF EVENTS/10°
80
60
40
20
0
0°
90°
180°
270°
360°
ΨH

Fig. 16

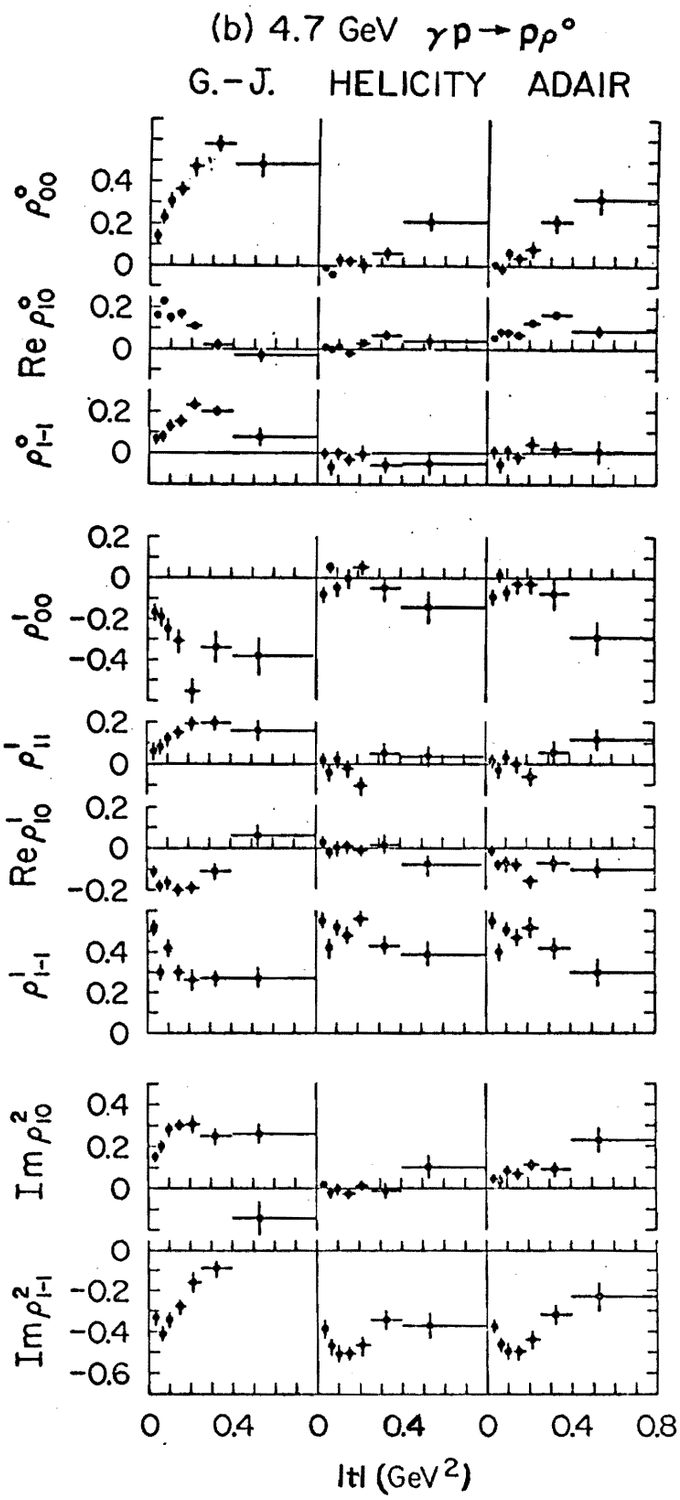
(b) 4.7 GeV γp → pρ°
G.-J. HELICITY ADAIR
ρ°00
Re ρ°10
ρ°1-1
ρ'00
ρ'11
Re ρ'10
ρ'1-1
Im ρ²10
Im ρ²1-1
0.4
0.2
0
-0.2
-0.4
-0.6
0.8
|t| (GeV²)

Fig. 17

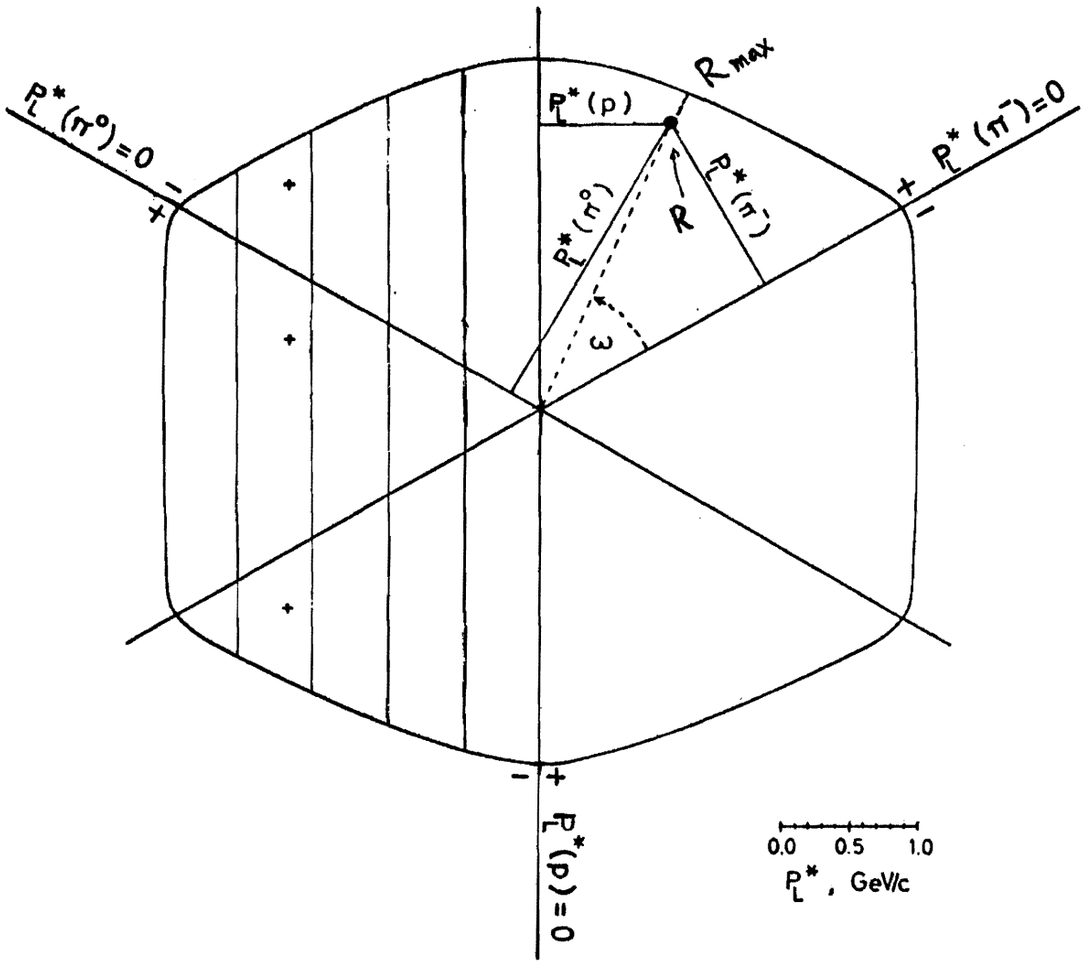

Fig. 18

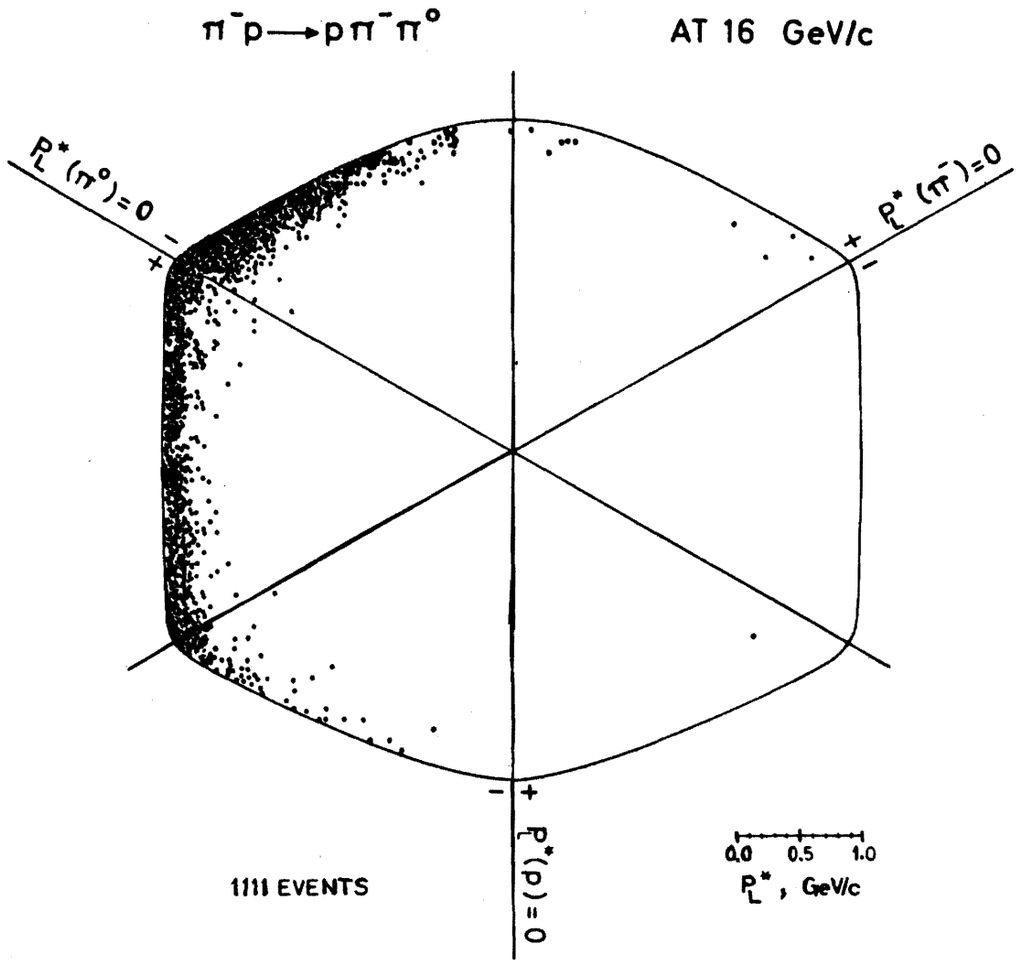

Fig. 19

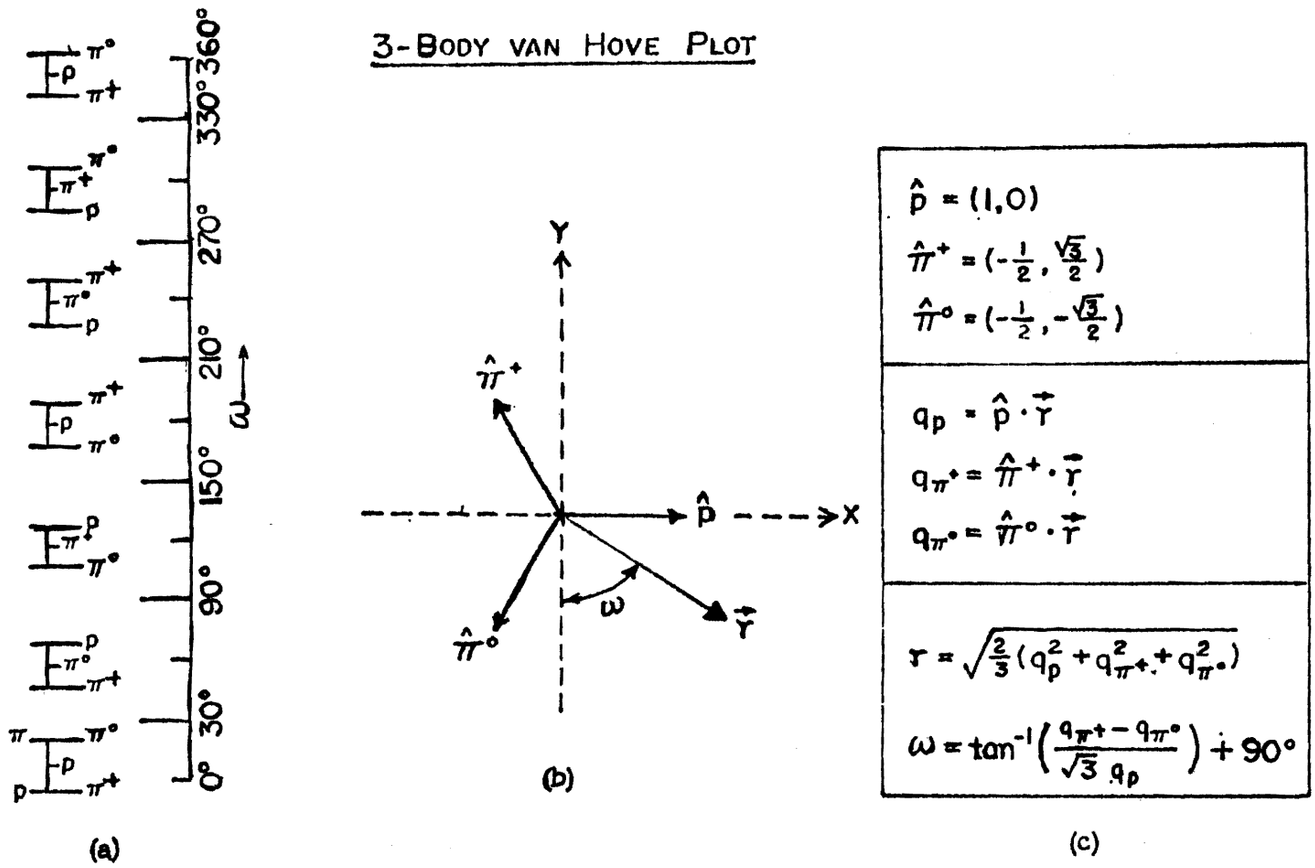
3-Body van Hove Plot
ρ π° π+
π+ π° p
π+ π° p
ρ π+ π°
π° p π+
π π° p π+
0° 30° 90° 150° 210° 270° 330° 360°
ω
(a)
Y
X
p̂
π̂+
π̂°
ω
r
(b)
p̂ = (1,0)
π̂+ = (-1/2, √3/2)
π̂° = (-1/2, -√3/2)
qp = p̂ · r
qπ+ = π̂+ · r
qπ° = π̂° · r
r = √(2/3 (qp² + qπ+² + qπ°²))
ω = tan⁻¹((qπ+ - qπ°)/(√3 qp)) + 90°
(c)
π+
p
R
Rmax
ω
π°
(d)
Tp
Tπ+
Tπ°
(e)

Fig. 20


Z
Y
X

(a)

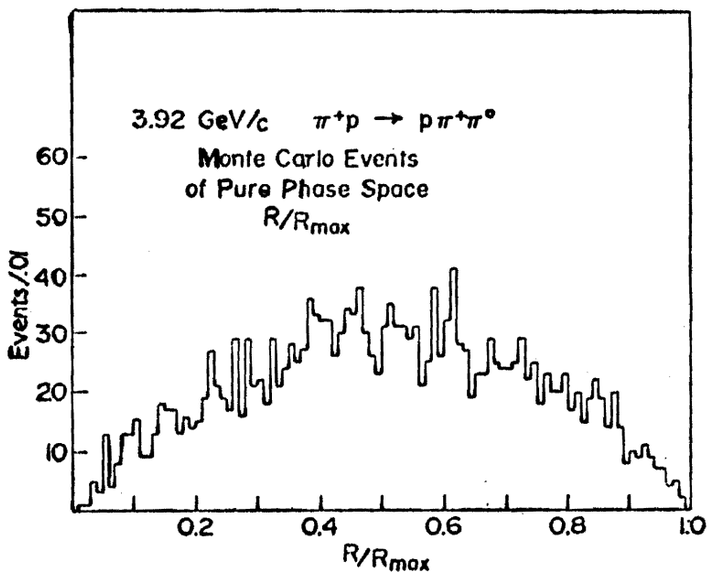
3.92 GeV/c π⁺p → pπ⁺π°
Monte Carlo Events
of Pure Phase Space
R/Rmax
Events/.01
60
50
40
30
20
10
0.2
0.4
0.6
0.8
1.0
R/Rmax

(b)


Z
2
1
2
Y
X

(c)

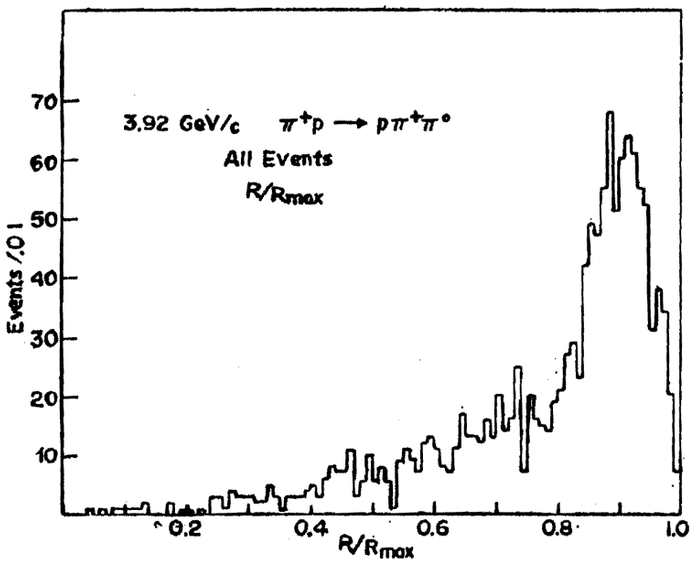
3.92 GeV/c π⁺p → pπ⁺π°
All Events
R/Rmax
Events/.01
70
60
50
40
30
20
10
0.2
0.4
0.6
0.8
1.0
R/Rmax

(d)

Fig. 21

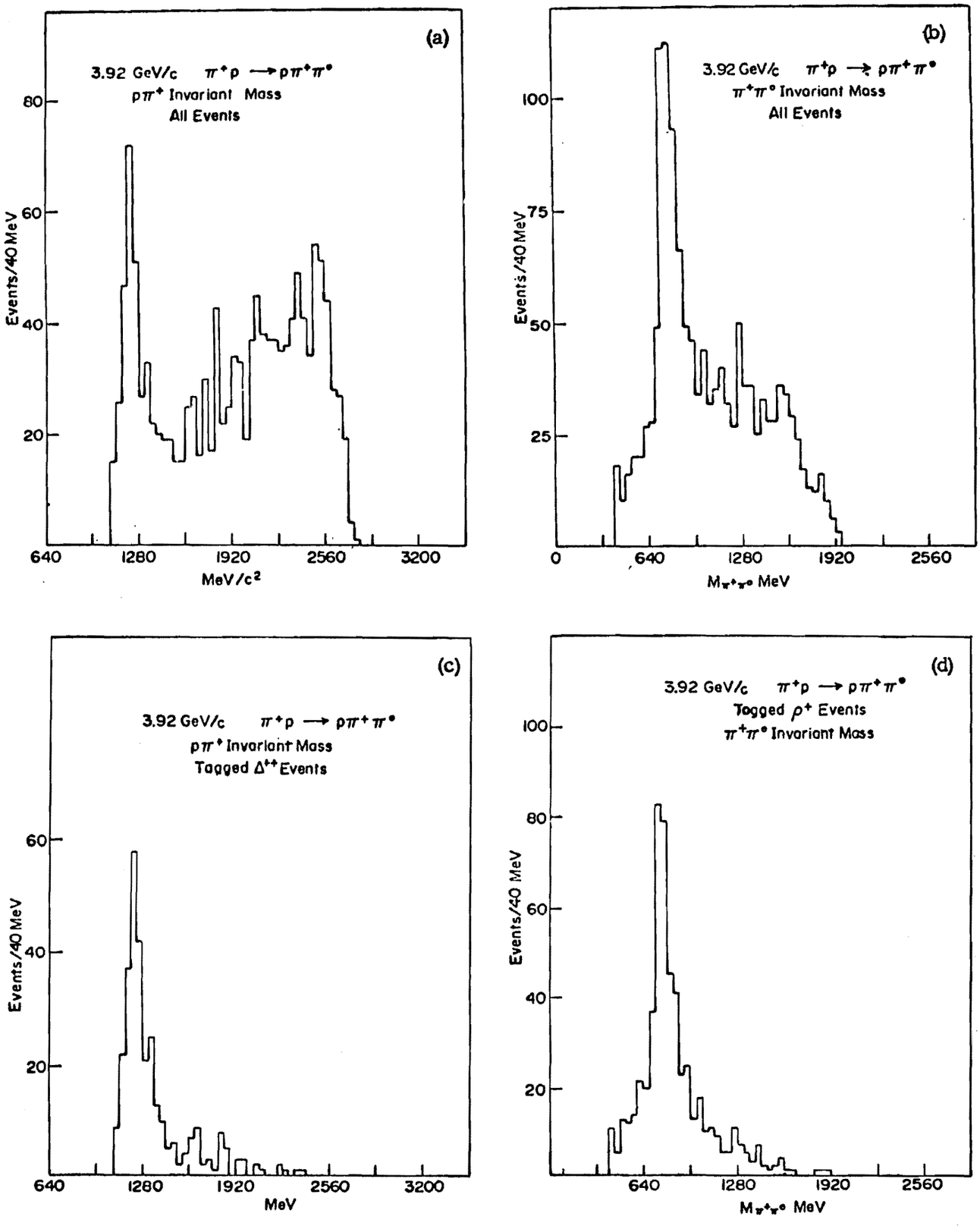
(a)
3.92 GeV/c $\pi^+p \rightarrow p\pi^+\pi^0$
$p\pi^+$ Invariant Mass
All Events
Events/40 MeV
MeV/c^2
(b)
3.92 GeV/c $\pi^+p \rightarrow p\pi^+\pi^0$
$\pi^+\pi^0$ Invariant Mass
All Events
Events/40 MeV
$M_{\pi^+\pi^0}$ MeV
(c)
3.92 GeV/c $\pi^+p \rightarrow p\pi^+\pi^0$
$p\pi^+$ Invariant Mass
Tagged Δ^{++} Events
Events/40 MeV
MeV
(d)
3.92 GeV/c $\pi^+p \rightarrow p\pi^+\pi^0$
Tagged ρ^+ Events
$\pi^+\pi^0$ Invariant Mass
Events/40 MeV
$M_{\pi^+\pi^0}$ MeV

Fig. 22